The Tutupaca volcanic complex (Southern Peru): Eruptive chronology and successive destabilization of a dacitic dome complex

J. Mariño, Pablo Samaniego, N. Manrique, P. Valderrama, Olivier Roche, Benjamin van Wyk de Vries, Herve Guillou, S. Zerathe, C. Arias, C. Liorzou

The Tutupaca volcanic complex (Southern Peru): Eruptive chronology and successive destabilization of a dacitic dome complex

J. . Mariño[a], P. Samaniego[b,*], N. Manrique[a], P. Valderrama[c], O. Roche[b], B. van Wyk de Vries[b], H. Guillou[d], S. Zerathe[e], C. Arias[a], C. Liorzou[f]

a Instituto Geológico Minero y Metalúrgico, Avenida Canada, 1470, San Borja, Lima, Perú
b Laboratoire Magmas et Volcans, Université Clermont Auvergne, CNRS, IRD, OPGC, F-63000, Clermont-Ferrand, France
c Departamento de Ingeniería, Pontificia Universidad Cat´olica del Perú, Lima, Perú
d Laboratoire des Sciences du Climat et de l'Environnement, LSCE/IPSL, CEA-CNRS-UVSQ, Université Paris-Saclay, F-91191, Gif-sur-Yvette, France
e ISTerre, Université Grenoble Alpes, Université Savoie Mont Blanc, CNRS, IRD, IFSTTAR, 38000, Grenoble, France
f Laboratoire Géosciences Océan, Institut Universitaire Européen de la Mer, Université de Bretagne Occidentale, Rue Dumont d'Urville, 29280, France

Several processes have been proposed as triggering mechanisms for the large sector collapses that affect most volcanoes, and which may occur several times in the volcano's lifetime. Here we present and discuss the case of Tutupaca volcano, located in southern Peru and part of the Central Volcanic Zone of the Andes. Tutupaca is composed of an old, hydrothermally altered and highly eroded Basal edifice, as well as younger twin peaks located in the northern part of the complex (the Western and Eastern Tutupaca). The youngest Eastern edifice of Tutupaca is composed of at least seven coalescing lava domes and associated deposits, including block-and-ash flow and debris avalanche deposits. We identified two debris avalanche deposits. An older unit (Azufre debris avalanche deposit) was channeled in the valleys located to the E and SE of the basal volcano, reaching up to 3.5 km from its source region. Four cosmogenic nuclide exposure dates (^{10}Be/feldspar) were obtained from boulders of this debris avalanche deposit and ranged between 6.0 $\pm$ 0.7 and 7.8 $\pm$ 1.5 ka. The younger unit (Paipatja deposit) was associated with the sector collapse of the edifice reconstructed just after the first debris avalanche (domes IV to VIII). The sector collapse produced a debris avalanche deposit that outcrops immediately to the NE of the amphitheater and was associated with a large pyroclastic density current deposit that was previously dated by radiocarbon at 218 $\pm$ 14 a BP (Samaniego et al., 2015). Both debris avalanche deposits have two contrasting sub-units: (1) the main subunit, hereafter called hydrothermal-altered debris avalanche deposit, is a whitish-yellow volcanic breccia with heterolithic and heterometric blocks, which originated from the Basal edifice, and (2) a dome-rich debris avalanche deposit, composed by non-altered dome blocks from Eastern Tutupaca. In proximal areas, the dome-rich unit overlaps the hydrothermally-altered unit while in distal areas, these two units are mixed forming a hummocky and/or ridged topography. In addition to the similarity of both debris avalanches, we propose that the triggering mechanism for these debris avalanches was similar. The dacitic dome growth, coupled with a substrate of older, hydrothermally-altered rock, induced the destabilization of the edifice, producing the debris avalanches and the related pyroclastic density currents.

1. Introduction

Reconstructing the eruptive chronology of potentially active volcanoes represents the first step of any volcanic hazard initiative. During the last two decades, the eruptive chronology of some Peruvian volcanoes has been studied in detail. These studies include some of the most active volcanoes of this part of the Andes, such as El Misti (Thouret et al., 2001), Ubinas (Thouret et al., 2005), Ampato-Sabancaya (Samaniego et al., 2016), and Yucamane (Rivera et al., 2020). In addition, previous work has been focused on some key eruptions that showed an importance by their size and their eruptive dynamics. This is the case of the large, 2 ka BP explosive eruption of El Misti volcano (Volcanic Explosive Index, VEI 5, Harpel et al., 2011; Cobeñas et al., 2012), and the 1600 CE explosive eruption of Huaynaputina volcano, which is considered the

* Corresponding author.
E-mail address: pablo.samaniego@ird.fr (P. Samaniego).

biggest historical eruption in the Andes (VEI 6, Thouret et al., 1999; Adams et al., 2001). The last eruption of Tutupaca volcano has also been studied in detail due to the fact that it probably represents the youngest debris avalanche in the Andes and was accompanied by one of the largest explosive events to have occurred in Southern Peru during historical times (218 ± 14 aBP, Samaniego et al., 2015; Valderrama et al., 2016; 2018; Manrique et al., 2020). However, very little is known of the whole eruptive chronology of this potentially active edifice, located 25–30 km north of Candarave village (Tacna Department, Southern Peru).

The eruptive chronology of most composite volcanoes consists of long-lasting growth cycles, punctuated by "rapid" collapse events affecting a single flank or the entire edifice. These destabilization events produce large volcanic landslides that usually transform into long run-out debris avalanches. As a result, the debris avalanche deposits spread out at the base of the volcano, leaving a horseshoe-shaped scar in the source region (van Wyk de Vries and Davis, 2015). The structure of most volcanic edifices, formed by an accumulation of lava and pyroclastic deposits, provide an intrinsic susceptibility to gravitationally-controlled collapse. The edifice's intrinsic weakness can be developed during its lifetime, which means that volcanic landslides are not necessarily related to volcanic activity. However, some short-term triggering mechanisms have also been invoked to explain the sudden edifice destabilization, as for instance: a shallow intrusion of a new batch of magma prior to the eruption (Hoblitt et al., 1981; Donnadieu and Merle, 1998); a change in the hydrothermal system induced by an increase of its pore fluids pressure (Reid et al., 2001; van Wyk de Vries et al., 2000); and/or seismic activity resulting from volcano-tectonic deformation (Lagmay et al., 2000; Vidal and Merle, 2000).

In the Central Andean context, volcanic debris avalanches are frequent, occurring at least once during most volcanoes' lifetime. Some well-known examples of large debris avalanche deposits have been described in Chile and Argentina at Socompa (van Wyk de Vries et al., 2001; Kelfoun et al., 2008), Parinacota (Clavero et al., 2002), and Llullaillaco volcanoes (Richards and Villeneuve, 2001); as well as in Peru at Pichu Pichu volcano (Legros et al., 2000; Bernard et al., 2019).

On the basis of a comprehensive study of this volcanic center that includes geological mapping coupled with geochronological and geochemical analyses, the first goal of this manuscript is to reconstruct the eruptive chronology of Tutupaca volcano from the Middle Pleistocene to Holocene. In addition, the new chronological data, along with previous studies focused on the last debris avalanche deposits of Tutupaca (Samaniego et al., 2015; Valderrama et al., 2016; Manrique et al., 2020) allow us to explain the recurrence of sector collapses that have affected this volcano during the Holocene.

2. Geological setting

Volcanic activity in the Andean Central Volcanic Zone (CVZ) has occurred at least since the Plio-Quaternary (de Silva and Francis, 1991) as a consequence of the subduction of the oceanic Nazca plate beneath the South American continental lithosphere. The volcanic arc extends along ~1000 km and mainly consists of calc-alkaline eruptive products, with a predominance of andesites, although more siliceous magmas are also present (Mamani et al., 2010). The CVZ in southern Peru comprises single stratovolcanoes (*e.g.* El Misti), compound volcanoes (*e.g.* Ampato-Sabancaya), dome complexes (*e.g.* Ticsani), large volcanic clusters (*e.g.* Chachani), and monogenetic fields (*e.g.* Huambo-Andagua-Orcopampa). Currently, there are at least ten active or potentially active volcanoes in the Peruvian segment of the CVZ, which erupted at least once during the Holocene (Fig. 1; De Silva and Francis, 1991; Siebert et al., 2011; Bromley et al., 2019). Among these edifices, at least five erupted during the historical time and thus are

Fig. 1. Location of Tutupaca volcano in the Peruvian volcanic arc.

considered as active. These edifices are Ubinas, Sabancaya, Tutupaca, El Misti and Huaynaputina.

Tutupaca volcanic center, hereafter referred to as Tutupaca (17° 01′S, 70° 21′W, 5790 m above sea level – asl, Fig. 1) is constructed on the Mesozoic and Cenozoic volcanic and sedimentary formations that compose the Western Cordillera of the Peruvian Andes (Sébrier and Soler, 1991). These formations include Jurassic to Cretaceous sandstones and carbonaceous shales of the Labra and Hualhuani Formations, which are covered by the volcanic sequences of the Cretaceous Toquepala Formation (De la Cruz and De la Cruz, 2000). Overlying these units are the volcanic and volcano-sedimentary sequences of the Mio-Pliocene (Figs. 2 and 3; Fidel and Zavala, 2001; Mamani et al., 2010). South of Tutupaca, these volcanic sequences consist of the dacitic and rhyolitic welded ignimbrites from the Miocene Huaylillas Formation that were dated by K–Ar to be 24-10 Ma (Tosdal et al., 1981; Quang et al., 2005). To the east and southeast of Tutupaca are outcrops of dacitic, non-welded, ignimbrite deposits of the Mio-Pliocene Capillune Formation (7-3 Ma, Tosdal et al., 1981; Martínez and Cervantes, 2003). Lastly, on top of this volcanic sequence, there are several eroded composite cones belonging to the Barroso Group (10–1 Ma, Mamani et al., 2010; Thouret et al., 2016). An andesitic lava sample from the Nazaparco volcano, located to the southeast of Tutupaca yielded a whole-rock K–Ar age of 5.6 ± 0.2 Ma (Martínez and Cervantes, 2003), in agreement with recent unspiked K–Ar ages obtained on Yucamane Chico volcano that range from 6.14 ± 0.11 Ma to 5.47 ± 0.09 Ma (Rivera et al., 2020).

In the southern part of the Peruvian volcanic arc, it has been identified an active fault system roughly parallel to the Andes, that corresponds to a series of NW-SE-trending normal faults with a sinistral component (Martínez and Cervantes, 2003; Benavente et al., 2010). Around Suches lake, 10 km to the north of Tutupaca, Benavente et al. (2010) identified several fault segments with an average N140° strike and a roughly SW dip angle. These faults are several kilometers long and show recent, 5–20 m, of cumulative vertical offsets, attesting its active character. The SE prolongation of these faults has been recently mapped at Tutupaca by Mariño et al. (2019), who named these segments as Banco, Azufre Grande and Western Tutupaca faults (Fig. 3).

Tutupaca was constructed on top of a high plateau at 4100–4600 m asl and covers an area of 150–170 km^2. It is composed of a large, highly eroded Basal edifice and two small twin peaks (Western and Eastern Tutupaca), which are located at the northern part of the volcanic complex and were constructed on the remnants of the basal volcano (Samaniego et al., 2015; Mariño et al., 2019, Figs. 2 and 3). Pleistocene glaciations strongly affected Tutupaca. Based on detailed glaciological studies performed in the Western Cordillera of the Peruvian Andes, as well as the comparison between the different moraines identified in some Peruvian volcanoes (Coropuna, Bromley et al., 2009; Ampato-Sabancaya, Samaniego et al., 2016; Hualca Hualca, Alcalá-Reygosa et al., 2017; Yucamane, Rivera et al., 2020), we consider that the larger moraines reaching lower altitudes were associated with the Last Glacial Maximum, which is roughly dated in the Peruvian Andes between 25 and 17 ka (Bromley et al., 2009; Alcalá-Reygosa et al., 2017). In contrast, the smaller moraines that reached higher altitudes, were associated with younger glacial advances such as the Younger Dryas event, which is dated at 12–10 ka (Clapperton, 1991; Alley, 2000; Zech et al., 2007).

The last eruption of Tutupaca was the focus of detailed studies by our group during the last few years. This eruption was characterized by a sector collapse of the younger Eastern Tutupaca dome complex that triggered a debris avalanche and an associated pyroclastic eruption, whose deposits have been dated by radiocarbon at 218 ± 14 aBP (Samaniego et al., 2015). In addition, due to a unique degree of preservation of the surface structures of these deposits, Valderrama et al. (2016, 2018) studied the dynamic process associated with this debris avalanche. Lastly, Manrique et al. (2020) performed a detailed petrological study of the last eruption products in order to constrain the magmatic process associated with the sector collapse. Given the importance of these results on the overall understanding of the triggering processes related with the Tutupaca sector collapses, we include in the forthcoming sections a summary of these works.

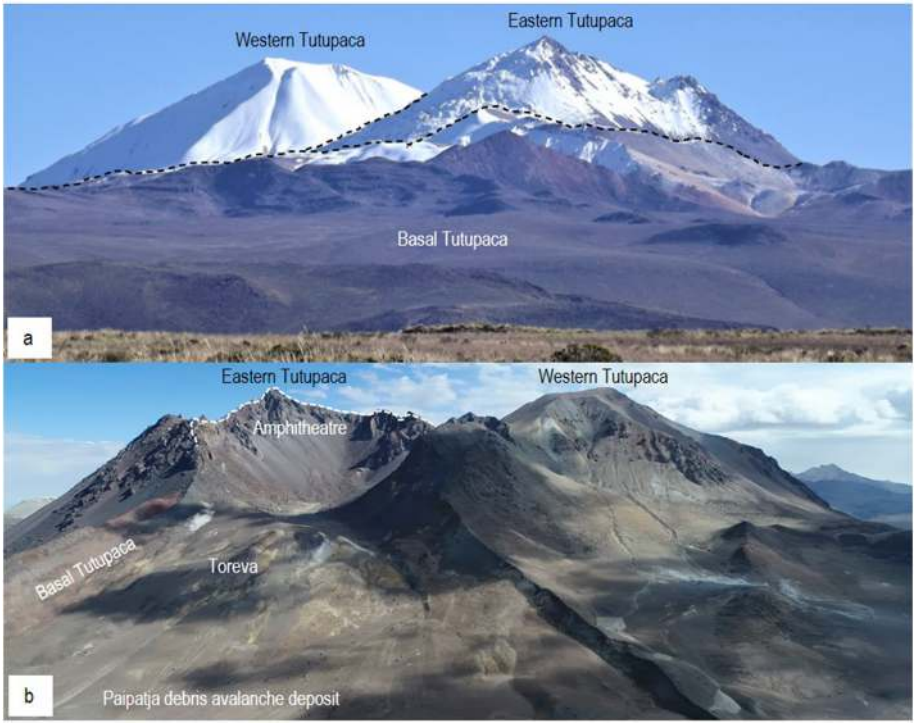

Fig. 2. **(a)** Panoramic view from the south of the Tutupaca volcanic complex. **(b)** Panoramic view from the north-east of Eastern and Western Tutupaca edifices and its recent amphitheatre.

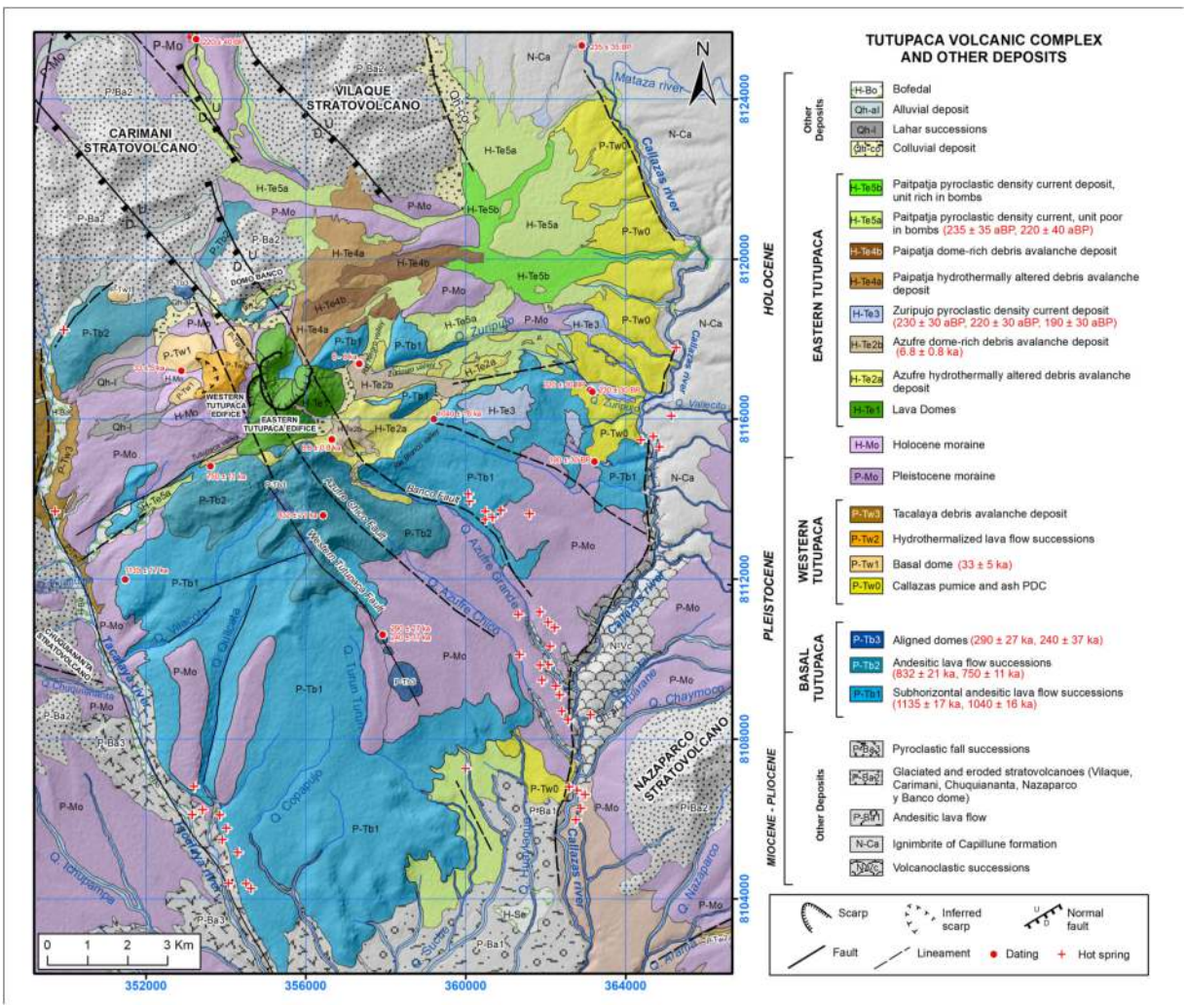

Fig. 3. Geological map of the Tutupaca volcanic complex.

3. Methodology

Fieldwork at Tutupaca volcano was carried out during several campaigns between 2012 and 2014. These studies included detailed geologic mapping and sampling of most volcanic units and were part of a comprehensive volcanological study of the complex. Here, we focus on the reconstruction of the eruptive chronology of the whole volcanic complex, based on new field, petrographic, geochemical and geochronological data. Major and trace element whole-rock analyses for Basal and Western Tutupaca (Table 1) were obtained from agate-crushed powders of a dataset of 52 new samples at the Laboratoire Géosciences Océan, Université de Bretagne Occidentale (Brest, France), using an Inductively Coupled Plasma-Atomic Emission Spectrometer (ICP-AES) and following the analytical procedure described by Cotten et al. (1995). Calibrations were performed using international standards (ACE, ME, WSE, JB2). Relative standard deviation (2 sigma) is $\leq$ 1% for SiO_2, $\leq$2% for the other major elements and $\leq$5% for trace elements. We also include in our dataset 37 analyses from the Eastern Tutupaca eruptive products, which were obtained at the same laboratory and were recently published by Manrique et al. (2020).

The chronology of the Pleistocene eruptive activity was established using the unspiked K–Ar method described in Guillou et al. (2011). Additional details of this method were recently published in Rivera et al. (2020). Five samples collected from Basal and Western Tutupaca were selected for K–Ar dating (Table 2). Holocene chronology of Tutupaca was constrained by cosmic ray exposure dating using the couple ^{10}Be/feldspar on four dacitic boulders from one of the identified debris avalanche deposits (Table 3). These samples were processed at the ISTerre GeoThermoChronology platform (Grenoble, France) following the chemical procedure of Zerathe et al. (2017), which is specific to feldspar. Measurement of ^{10}Be/^{9}Be ratios were carried out at the French National AMS facility ASTER (Arnold et al., 2010, 2013) located at the CEREGE laboratory (Aix-en-Provence, France), and calibrated against the "in-house standard" with an assumed ^{10}Be/^{9}Be ratio of 1.191 $\pm$ 0.013 $\times$ 10^{-11} (Braucher et al., 2015). Analytical uncertainties include the counting statistics, the machine stability (~0.5%, Arnold et al., 2010) and the blank correction whose ^{10}Be/^{9}Be value was 8.01 $\pm$ 0.60 $\times$ 10^{-16} (Table 3). Exposure ages were calculated using the CREp program (Martin et al., 2017; Supplementary Material). We applied the Lifton-Sato-Dunai scaling model (Lifton et al., 2014), the ERA40 atm model and time-dependent corrections from the Lifton (2016) geomagnetic databases. We used the ^{10}Be production rate in feldspar of 3.57 $\pm$ 0.21 at $g^{-1}.yr^{-1}$ from Zerathe et al. (2017). This value corresponds to a regional calibration of ^{10}Be in feldspar against the ^{3}He production rate in pyroxene averaged for the High Tropical Andes (Zerathe et al., 2017). Because local constraints on denudation rates do not exist in the studied region, a zero-denudation rate was assumed. Exposure ages should thus be considered as minimum ages. Lastly, additional constraints on the Holocene eruptive chronology of Tutupaca were obtained by five radiocarbon ages obtained from charcoal samples collected in pyroclastic deposits associated with the younger pyroclastic event (Samaniego et al., 2015), and one new peat sample collected on a

Table 1
Whole-rock major (wt.%) and trace (ppm) elements for the sampled of the Tutupaca. The unit code meaning come from Fig. 3. E – enclave, LD - lava dome, LF - lava flow, DAD - debris avalanche deposit, TF - tephra fallout, PDC - pyroclastic density current.

Sample No.	TU-12-24B	TU-12-25B	TU-12-24A	TU-12-25A	TU-13-05	TU-13-06B	TU-13-07	TU-12-64B	TU-13-33A	TU-13-33F	TU-13-36A	TU-13-36F	TU-12-13A	TU-12-13B	TU-12-29	TU-12-30	TU-12-31
Unit	P-Tw1	P-Tw1	P-Tw1	P-Tw1	P-Tw1	P-Tw1	P-Tw1	P-Tw3	P-Tw	P-Tw	P-Tw	P-Tw	P-Tw	P-Tw	P-Tw	P-Tw	P-Tw
Description	E	E	LD	LD	LD	LD	LD	DAD	TF	TF	TF	TF	PDC	PDC	PDC	PDC	PDC
North	8118313	8117773	8118313	8117773	8117211	8116794	8117625	8114478	8085755	8085755	8085616	8085616	8115884	8115884	8116501	8119038	8106835
East	354077	352447	354077	352447	352891	353035	354675	349870	360427	360427	364645	364645	363339	363339	363910	364877	362023
Altitude	5213	4965	5213	4965	5154	5232	5446	4542	3178	3178	3500	3500	4464	4464	4399	4430	4142
SiO2 (wt.%)	54.2	53.5	63.2	64.0	62.2	66.0	63.1	66.1	58.8	67.0	59.2	64.0	57.6	63.5	64.7	66.0	62.8
TiO2	1.3	1.4	0.7	0.7	0.8	0.6	0.7	0.6	0.9	0.5	0.9	0.5	0.9	0.5	0.5	0.5	0.6
Al2O3	16.9	16.7	15.5	15.3	15.6	15.5	15.5	15.5	16.4	14.4	16.6	14.3	17.7	15.5	14.8	14.3	16.2
Fe2O3*	8.6	9.1	4.9	4.7	5.2	4.2	4.4	3.6	6.2	3.1	6.1	3.5	6.3	3.8	3.8	3.4	4.5
MnO	0.1	0.1	0.1	0.1	0.1	0.1	0.1	0.1	0.1	0.1	0.1	0.1	0.1	0.1	0.1	0.1	0.3
MgO	3.8	4.2	2.0	1.8	2.3	1.5	1.9	1.3	2.6	1.4	2.5	1.4	1.6	1.3	1.3	1.3	1.3
CaO	7.3	7.8	4.3	4.1	4.7	3.6	3.9	3.6	5.3	2.8	5.2	2.9	4.8	3.2	3.1	2.8	2.6
Na2O	3.7	3.6	4.1	4.1	4.0	4.0	3.7	4.2	3.7	3.2	2.7	3.7	3.6	3.1	3.2	3.2	2.7
K2O	2.2	2.1	3.0	3.0	2.9	3.5	3.3	3.3	2.6	4.3	2.7	3.7	2.7	3.9	4.1	4.4	3.8
P2O5	0.4	0.4	0.2	0.2	0.3	0.3	0.3	0.3	0.3	0.2	0.3	0.2	0.3	0.2	0.2	0.2	0.0
LOI	0.7	−0.1	0.8	0.4	0.8	0.6	1.8	0.4	3.7	3.8	3.8	4.1	3.2	3.3	2.9	3.3	4.5
Total	99.1	99.0	98.8	98.4	98.8	99.8	98.6	98.9	100.5	100.7	100.0	98.4	98.7	98.3	98.6	99.4	99.3
Sc (ppm)	17.3	19.9	8.8	7.7	10.9	4.9	8.8	5.8	11.1	6.2	10.6	6.9	11.4	6.7	6.6	5.8	9.7
V	212.5	231.5	110.6	103.3	116.3	83.7	99.3	74.0	143.5	59.0	140.8	67.5	118.6	71.8	74.9	64.7	94.2
Cr	21.0	27.6	13.2	13.1	13.6	7.4	14.2	14.9	4.8	7.5	5.5	10.5	10.5	12.2	12.9	9.6	16.4
Co	19.4	20.7	11.6	10.7	12.0	11.1	11.9	9.5	19.5	8.0	17.9	9.0	15.4	9.6	8.8	7.9	21.9
Ni	8.4	9.0	8.2	6.8	8.9	8.9	10.1	8.3	15.8	8.5	15.7	8.7	13.8	7.6	9.9	6.9	11.9
Rb	60.9	47.2	91.1	98.6	77.4	108.3	98.6	96.0	60.8	115.2	63.7	110.5	80.3	145.0	141.8	163.7	157.3
Sr	938.1	895.2	647.8	638.6	698.0	643.7	627.1	735.9	772.3	419.9	774.3	442.6	811.2	493.5	455.0	410.9	413.4
Y	22.5	25.9	12.2	11.5	14.7	9.8	12.0	8.8	13.9	14.0	13.9	14.0	11.6	13.6	13.2	12.3	13.5
Zr	146.9	161.7	86.4	79.2	87.5	60.5	82.4	88.1	176.5	148.1	165.4	152.1	172.0	144.4	147.9	154.8	171.8
Nb	8.4	7.2	6.6	6.6	8.5	7.7	7.9	8.3	7.7	9.0	8.3	10.3	7.8	9.1	8.6	8.7	9.2
Ba	885.0	833.0	1010.7	976.1	951.1	1104.2	1037.7	1104.7	1032.0	937.5	1003.2	954.1	1011.1	911.6	872.8	963.6	1063.7
La	27.0	28.1	29.2	32.4	30.0	29.5	29.2	33.7	31.5	33.2	31.6	33.7	29.7	33.1	32.8	33.0	30.4
Ce	59.5	59.7	59.3	59.8	60.8	51.4	55.0	65.9	63.7	65.4	63.9	67.1	59.8	63.1	64.0	64.4	59.1
Nd	29.6	31.6	24.5	23.5	26.0	22.0	23.2	25.3	28.8	25.2	28.8	25.6	25.1	25.0	24.8	24.0	23.6
Sm	6.0	6.3	4.8	4.9	5.0	4.1	4.1	4.3	5.2	4.6	5.2	4.4	4.7	4.0	4.6	3.6	4.4
Eu	1.6	1.8	1.1	1.1	1.3	1.1	1.1	1.3	1.3	0.8	1.3	0.9	1.1	1.0	1.0	0.9	0.9
Gd	5.3	6.1	3.5	3.3	3.9	3.0	3.4	2.9	4.2	3.5	4.0	3.3	3.6	3.5	3.4	3.3	3.1
Dy	3.9	4.5	2.3	2.3	2.7	2.0	2.3	1.8	2.6	2.5	2.7	2.4	2.1	2.3	2.4	2.1	2.4
Er	2.1	2.0	1.3	0.8	1.5	0.7	1.7	0.7	1.5	1.2	1.4	1.4	1.1	1.5	1.1	1.1	1.3
Yb	1.8	2.2	0.9	0.9	1.2	0.7	1.0	0.7	1.1	1.2	1.1	1.3	0.9	1.2	1.3	1.1	1.3
Th	4.3	3.6	9.7	10.3	10.3	9.7	11.4	9.6	6.1	15.5	6.2	15.5	6.7	14.6	14.2	15.2	13.0

Sample No.	TU-12–35A	TU-12–35B	TU-12–86B	TU-12–90	TU-12–98B	TU-12–62	TU-12–03	TU-12–07	TU-12–10	TU-12–15	TU-12–20	TU-12–21	TU-12–23	TU-12–26	TU-12–44	TU-12–48	TU-12–60
Unit	P-Tw	P-Tw	P-Tw	P-Tw	P-Tw	P-Tw	P–Tb1	P–Tb1	P–Tb1	P–Tb1	P–Tb1	P–Tb1	P–Tb1	P–Tb1	P–Tb1	P–Tb1	P–Tb1
Description	PDC	PDC	PDC	PDC	PDC	TF	LF	LF	LF	LF	LF	LF	LF	LF	LF	LF	LF
North	8122931	8122931	8108017	8107669	8106739	8110688	8118706	8116249	8118273	8117345	8115995	8116003	8119278	8106270	8116940	8118137	8114792
East	364348	364348	360665	361130	362023	361595	354946	363137	358237	356816	357968	359208	352791	353926	355317	356708	352028
Altitude	4445	4445	4184	4144	4145	4347	5107	4498	4867	5020	4996	4798	4934	4223	5376	4990	4782
SiO2 (wt.%)	66.6	59.1	65.8	67.1	61.0	63.6	64.1	61.9	62.4	57.3	61.2	60.9	63.3	57.8	65.6	67.2	60.9
TiO2	0.5	0.9	0.5	0.5	0.6	0.5	0.6	0.7	0.8	0.8	0.9	0.7	0.8	0.9	0.7	0.4	0.7
Al2O3	14.2	17.1	15.0	15.9	17.6	15.4	16.3	16.0	16.3	18.1	16.2	17.4	15.8	17.4	15.1	15.7	17.0

(*continued on next page*)

Table 1 (*continued*)

Sample No.	TU-12–35A	TU-12–35B	TU-12–86B	TU-12–90	TU-12–98B	TU-12–62	TU-12–03	TU-12–07	TU-12–10	TU-12–15	TU-12–20	TU-12–21	TU-12–23	TU-12–26	TU-12–44	TU-12–48	TU-12–60
Unit	P-Tw	P-Tw	P-Tw	P-Tw	P-Tw	P-Tw	P–Tb1	P–Tb1	P–Tb1	P–Tb1	P–Tb1	P–Tb1	P–Tb1	P–Tb1	P–Tb1	P–Tb1	P–Tb1
Description	PDC	PDC	PDC	PDC	PDC	TF	LF	LF	LF	LF	LF	LF	LF	LF	LF	LF	LF
North	8122931	8122931	8108017	8107669	8106739	8110688	8118706	8116249	8118273	8117345	8115995	8116003	8119278	8106270	8116940	8118137	8114792
East	364348	364348	360665	361130	362023	361595	354946	363137	358237	356816	357968	359208	352791	353926	355317	356708	352028
Altitude	4445	4445	4184	4144	4145	4347	5107	4498	4867	5020	4996	4798	4934	4223	5376	4990	4782
Fe2O3*	3.4	6.3	3.8	3.5	4.0	4.3	4.2	5.2	5.1	6.3	5.1	5.2	5.0	7.2	4.2	3.0	5.8
MnO	0.1	0.1	0.1	0.0	0.1	0.0	0.1	0.1	0.1	0.1	0.1	0.1	0.1	0.1	0.0	0.0	0.1
MgO	1.2	2.6	1.1	1.0	1.1	0.9	1.6	2.3	2.2	2.5	2.1	2.3	2.0	3.1	1.3	0.9	2.3
CaO	2.9	5.4	2.1	1.9	2.4	2.6	3.7	4.8	4.6	6.1	4.5	5.6	3.9	6.6	3.1	2.9	5.1
Na2O	3.3	4.1	2.8	2.6	2.7	2.6	4.4	3.9	4.3	4.2	4.1	4.2	4.0	3.7	4.1	3.8	3.8
K2O	4.3	2.5	4.0	4.0	3.4	3.6	3.1	2.9	3.1	2.0	3.0	2.4	3.2	2.1	3.4	3.7	2.7
P2O5	0.2	0.3	0.0	0.0	0.1	0.0	0.2	0.2	0.3	0.3	0.3	0.2	0.3	0.2	0.2	0.1	0.2
LOI	2.5	1.3	4.6	5.2	7.1	5.3	0.4	1.2	0.0	0.8	1.4	0.2	0.4	0.8	0.5	0.6	1.0
Total	99.0	99.7	99.8	101.8	99.9	98.8	98.8	99.1	99.1	98.5	98.8	99.2	98.9	100.0	98.3	98.2	99.7
Sc (ppm)	6.5	11.6	6.6	8.7	8.3	7.6	5.8	9.4	9.4	11.4	8.9	10.3	7.7	17.3	5.8	5.9	13.7
V	67.7	147.3	72.6	68.0	73.3	76.2	93.6	112.4	111.6	163.8	119.5	117.8	105.3	183.5	77.9	50.8	131.3
Cr	10.5	5.0	13.2	9.3	14.9	16.7	15.8	39.6	35.6	10.5	37.2	50.1	21.8	30.1	9.8	20.0	18.9
Co	13.3	27.4	14.5	6.1	17.2	7.7	11.0	18.7	14.5	18.6	13.7	16.1	13.8	21.6	9.3	6.2	17.5
Ni	7.0	16.1	8.3	6.4	9.0	6.8	13.5	25.1	21.9	18.1	21.6	24.4	16.2	22.2	8.7	7.6	19.5
Rb	127.3	64.0	161.5	162.2	137.8	114.7	94.4	88.6	98.4	46.7	98.5	70.8	109.0	56.2	96.7	148.9	85.2
Sr	425.6	801.7	372.4	301.4	416.9	443.1	699.3	648.5	807.3	827.9	768.4	794.8	671.0	645.2	691.5	485.6	668.3
Y	13.3	17.1	13.3	11.0	14.7	12.2	7.3	17.8	12.8	11.7	10.0	10.9	12.2	18.0	4.6	17.6	14.7
Zr	152.5	172.1	151.7	152.2	178.5	158.0	133.8	128.5	158.6	149.6	78.0	128.5	106.6	131.3	78.4	142.3	135.2
Nb	9.1	7.9	9.3	9.1	10.6	10.1	6.1	7.0	8.2	5.0	9.3	5.9	9.2	5.4	7.9	8.2	7.5
Ba	916.3	1007.1	878.1	889.2	833.1	764.0	1055.4	940.2	1125.2	873.4	1077.3	850.7	1071.3	696.6	1213.5	1022.4	858.9
La	32.7	35.2	28.9	26.7	35.5	27.8	31.7	29.1	36.3	23.0	32.1	25.3	35.3	21.2	19.7	31.8	27.9
Ce	64.2	71.4	51.0	51.8	74.3	55.1	61.7	57.2	72.2	46.3	62.4	48.2	69.5	45.0	35.2	66.0	55.5
Nd	24.2	32.5	21.0	20.6	28.1	21.8	23.9	27.1	29.6	21.4	27.1	22.0	28.8	22.3	14.1	24.5	24.9
Sm	4.6	6.0	4.0	3.9	4.9	4.0	4.1	5.5	5.4	4.4	5.4	4.4	4.9	4.7	2.7	4.1	4.7
Eu	1.0	1.5	0.9	0.8	1.0	0.9	1.0	1.3	1.2	1.2	1.3	1.2	1.3	1.2	1.1	0.9	1.2
Gd	3.2	4.6	3.8	3.0	4.0	2.8	2.8	4.6	3.8	3.1	3.7	3.6	4.1	4.4	1.7	3.6	3.7
Dy	2.4	3.1	2.5	2.2	2.8	2.2	1.5	3.1	2.3	2.0	2.2	2.1	2.5	3.1	0.9	2.6	2.7
Er	1.0	1.2	1.5	1.5	1.4	0.8	0.2	2.1	0.9	1.5	0.8	0.9	0.7	1.5	0.3	1.4	1.3
Yb	1.3	1.3	1.4	1.2	1.4	1.2	0.7	1.3	1.0	1.0	0.8	0.8	0.9	1.4	0.4	1.3	1.2
Th	15.1	5.4	15.7	15.5	17.5	14.2	8.4	9.9	11.1	3.3	8.0	6.7	10.8	5.0	6.4	14.6	7.5

Sample No.	TU-12–82	TU-12–85	TU-12–89	TU-12–91	TU-12–93	TU-12–94	TU-12–95	TU-13–03	TU-13–04	TU-12–51	TU-12–56	TU-12–57	TU-12–63	TU-12–88	TU-12–32	TU-12–34	TU-12–65	TU-12–67
Unit	P–Tb1	P–Tb1	P–Tb1	P–Tb1	P–Tb1	P–Tb1	P–Tb1	P–Tb1	P–Tb1	P–Tb2	P–Tb2	P–Tb2	P–Tb2	P–Tb2	P–Tb3	P–Tb3	P–Tb3	P–Tb3
Description	LF	LF	LF	LF	LF	LF	LF	LF	LF	LF	LF	LF	LF	LF	LD	LD	LD	LD
North	8106546	8108234	8118052	8113613	8111990	8110851	8110282	8117655	8116905	8113757	8114822	8113593	8112031	8119916	8109344	8110204	8112061	8111255
East	359610	360427	351608	351574	351484	351961	352258	359432	358834	358851	353619	356438	356653	353528	358872	357980	356679	357213
Altitude	4180	4257	4881	4612	4619	4505	4438	4735	4805	4683	4918	5012	4933	4078	4521	4649	4940	4808
SiO2 (wt.%)	61.6	62.7	63.7	62.4	60.2	62.8	61.6	64.2	61.8	61.1	61.1	60.5	60.8	63.1	61.7	66.6	65.6	60.5
TiO2	0.7	0.8	0.8	0.7	0.8	0.8	0.8	0.7	0.8	0.7	0.9	0.7	0.7	0.8	0.7	0.5	0.6	0.7
Al2O3	17.3	16.6	15.9	16.8	16.8	17.4	17.1	16.5	16.9	16.7	16.9	15.9	17.5	16.4	16.8	15.6	15.4	17.1
Fe2O3*	5.3	5.4	5.4	4.9	5.6	5.5	5.8	4.5	5.1	4.6	5.1	5.9	5.3	5.2	5.3	3.4	3.4	5.2
MnO	0.1	0.1	0.1	0.1	0.1	0.1	0.1	0.1	0.1	0.1	0.1	0.1	0.1	0.1	0.1	0.1	0.0	0.1
MgO	2.4	2.3	2.1	2.0	2.6	2.3	2.9	2.1	2.4	2.2	2.4	2.9	2.5	2.0	2.1	1.3	1.3	2.7
CaO	4.9	4.8	4.2	4.6	5.2	5.1	5.5	4.4	4.9	4.8	5.2	5.0	5.7	4.4	4.7	3.3	3.3	5.8
Na2O	3.7	3.9	4.0	3.9	3.9	4.1	3.8	4.2	4.0	3.9	4.1	3.4	4.1	4.1	3.8	3.2	4.2	3.9

(*continued on next page*)

Table 1 (*continued*)

Sample No.	TU-12–82	TU-12–85	TU-12–89	TU-12–91	TU-12–93	TU-12–94	TU-12–95	TU-13–03	TU-13–04	TU-12–51	TU-12–56	TU-12–57	TU-12–63	TU-12–88	TU-12–32	TU-12–34	TU-12–65	TU-12–67
Unit	P–Tb1	P–Tb1	P–Tb1	P–Tb1	P–Tb1	P–Tb1	P–Tb1	P–Tb1	P–Tb1	P–Tb2	P–Tb2	P–Tb2	P–Tb2	P–Tb2	P–Tb3	P–Tb3	P–Tb3	P–Tb3
Description	LF	LF	LF	LF	LF	LF	LF	LF	LF	LF	LF	LF	LF	LF	LD	LD	LD	LD
North	8106546	8108234	8118052	8113613	8111990	8110851	8110282	8117655	8116905	8113757	8114822	8113593	8112031	8119916	8109344	8110204	8112061	8111255
East	359610	360427	351608	351574	351484	351961	352258	359432	358834	358851	353619	356438	356653	353528	358872	357980	356679	357213
Altitude	4180	4257	4881	4612	4619	4505	4438	4735	4805	4683	4918	5012	4933	4078	4521	4649	4940	4808
K2O	3.2	2.9	3.1	2.8	2.8	2.8	2.7	3.2	3.0	2.9	2.7	2.9	2.4	3.2	3.3	3.3	3.2	2.5
P2O5	0.2	0.2	0.3	0.2	0.2	0.2	0.2	0.2	0.3	0.2	0.3	0.2	0.2	0.3	0.2	0.2	0.2	0.2
LOI	1.1	0.2	0.2	0.4	0.8	0.1	0.7	0.1	0.4	1.3	0.5	1.6	0.8	0.2	0.8	1.7	1.6	0.7
Total	100.5	99.9	99.9	98.7	99.1	101.3	101.2	100.3	99.7	98.6	99.3	99.2	99.9	99.8	99.4	99.1	98.8	99.3
Sc (ppm)	11.4	10.6	8.2	10.6	13.0	11.9	12.8	9.3	9.6	10.1	12.0	12.4	12.8	8.2	9.9	4.8	5.3	12.9
V	115.3	128.3	109.9	114.0	143.7	131.6	144.7	98.7	111.7	107.8	117.0	135.3	125.9	108.9	111.8	67.5	70.6	113.8
Cr	27.9	53.5	15.8	31.2	39.3	39.4	45.6	24.2	47.1	40.7	50.0	78.7	20.3	15.4	29.7	12.3	12.2	23.4
Co	15.2	16.6	15.1	14.2	15.8	17.0	16.6	13.7	16.0	14.0	14.7	18.4	15.5	14.5	13.8	7.1	8.5	15.8
Ni	18.2	25.4	15.1	18.8	19.9	21.6	21.2	20.1	26.4	21.7	24.3	34.9	17.6	16.0	17.7	10.0	8.8	18.8
Rb	91.7	98.4	103.5	103.9	90.2	91.1	86.3	95.4	88.3	92.1	79.6	105.2	71.4	109.8	93.4	106.4	93.7	73.7
Sr	649.9	620.7	702.1	613.7	673.6	640.5	676.1	739.7	742.5	714.4	801.8	620.7	727.3	737.4	633.0	664.1	682.0	737.0
Y	16.6	17.6	14.5	13.1	15.0	14.4	15.4	12.8	15.0	14.4	14.2	13.2	12.3	12.6	19.2	7.6	7.0	12.9
Zr	176.8	150.1	151.2	132.1	159.2	163.3	157.9	150.9	151.4	98.6	114.4	141.8	136.7	121.7	169.8	127.7	137.4	137.8
Nb	9.5	8.1	9.3	7.7	7.7	7.8	7.2	8.6	8.4	8.2	8.3	6.8	6.2	9.0	9.6	7.2	7.2	7.3
Ba	1000.1	872.6	1001.0	858.0	846.7	899.9	794.0	1070.9	981.9	860.1	929.3	777.3	783.0	1046.5	1051.8	1052.2	1065.2	804.1
La	34.9	32.2	36.0	28.2	29.2	26.4	24.0	34.1	30.3	29.4	30.7	24.6	23.6	35.5	36.3	31.5	30.0	25.5
Ce	68.4	63.5	71.0	54.7	58.8	54.8	50.1	67.4	62.5	61.4	65.1	52.8	47.7	71.5	75.1	62.5	58.2	53.0
Nd	31.2	29.4	32.3	25.1	26.7	24.7	25.4	28.3	29.3	26.6	29.5	22.6	20.8	31.5	31.5	24.4	22.6	23.7
Sm	5.5	5.5	5.8	4.8	5.1	4.5	4.9	4.8	5.2	5.0	5.7	4.1	4.0	5.4	6.1	4.0	3.9	4.6
Eu	1.3	1.2	1.3	1.2	1.2	1.2	1.1	1.0	1.4	1.1	1.3	1.0	1.1	1.4	1.3	1.1	1.0	1.2
Gd	4.6	4.5	4.5	4.2	4.3	3.9	4.2	3.9	4.2	3.7	3.9	3.5	2.8	4.2	4.7	2.7	2.5	3.1
Dy	3.0	3.0	2.9	2.6	2.9	2.7	2.9	2.3	2.8	2.5	2.7	2.2	2.3	2.7	3.3	1.5	1.4	2.3
Er	1.8	1.7	1.8	1.5	1.6	1.4	1.8	1.2	1.1	1.1	1.0	1.1	1.0	1.5	1.1	0.0	0.4	1.2
Yb	1.5	1.4	1.2	1.2	1.3	1.3	1.3	1.1	1.2	1.2	1.1	1.2	1.0	1.1	1.5	0.6	0.6	1.1
Th	10.2	7.5	10.3	8.4	9.3	7.8	7.1	11.2	9.4	11.0	9.2	9.7	6.4	10.5	10.9	11.2	11.0	6.8

Table 2
K–Ar ages for rocks from the Tutupaca volcanic complex. The ages considered in the text are the weighted mean ages (in bold).

Sample number	Experiment number	Volcano	Unit and location	UTM Easting	UTM Northig	Altitude (m asl)	Split K (wt% ± 2σ)	Mass Molten (g)	^{40}Ar*%	^{40}Ar*10^{-11} (mol./g) ± 1σ	Weighted mean 40Ar*10^{-11} (mol./g) ± 1σ	Age (ka) ± 2σ
TU-12-93	71	Basal Tutupaca	P-Tb1. lava flow. S flank	351484	8111990	4619	3.121 ± 0.031	0.50691	49.092	6.044 ± 0.033		
	75							0.51394	51.014	6.234 ± 0.032	6.143 ± 0.023	**1135 ± 17**
TU-12-21	47	Basal Tutupaca	P-Tb1. lava flow. E flank	359208	8116003	4798	2.773 ± 0.028	0.50348	55.389	5.160 ± 0.038		
	54							0.50738	57.307	4.919 ± 0.027	5.000 ± 0.022	**1040 ± 16**
TU-12-56	66	Basal Tutupaca	P-Tb2. lava flow. W flank	353619	8114822	4918	2.881 ± 0.029	0.50161	46.046	3.798 ± 0.022		
	74							0.49886	50.715	3.709 ± 0.019	3.748 ± 0.015	**750 ± 11**
TU-12-57	67	Basal Tutupaca	P-Tb2. lava flow. S flank	356438	8113593	5012	2.665 ± 0.027	0.4942	15.183	3.845 ± 0.024		**832 ± 21**
TU-13-05	171	Western Tutupaca	P-Tw1. lava dome. W flank	352891	8117211	5154	2.764 ± 0.027	0.52251	0.206	0.175 ± 0.024		
	178							0.44054	0.17	0.149 ± 0.024	0.160 ± 0.017	**33 ± 5**

tephra succession located to the south-east of the complex. These samples were analyzed at the Center for Isotope Research (CIO), Groningen University (Netherlands).

4. The eruptive chronology of Tutupaca volcanic complex

4.1. Basal Tutupaca edifice

The Basal edifice, between 4100 and 5300 m asl, is mostly composed of two successive lava flows successions. The geometrical reconstruction of this edifice, based on the radial distribution of the lava flows, suggests the summit was located at the same location as the present one, and reached an altitude of 5400 m asl. The lavas are highly eroded and buried by moraine deposits, likely associated with the Last Glacial Maximum. We also identified several small lava domes in the NNW-SSE direction (Fig. 3). It is worth noting that the upper part of this edifice is characterized by widespread alteration that has been interpreted as a result of an active hydrothermal system (Steinmüller, 2001; Cruz and Matsuda, 2015) with some surface manifestations that include high-temperature, neutral-chloride and acid-sulphate waters (Azufre Grande, Tacalaya and Callazas hot-springs, Fig. 3). A recent X-ray diffraction characterization of a highly altered Basal Tutupaca sample confirmed the presence of an advanced argillic mineral assemblage, which is associated with steam-heated alteration processes (Detienne, 2016).

4.1.1. Lava flow successions

The older lava flow succession (P–Tb1, Figs. 3 and 4a) corresponds to sub-horizontal lava flows (~15–20°) that crop out at the southern, eastern and northwestern flanks of the complex between 4100 and 4800 m asl (Fig. 3). These lavas overlie the Mio-Pliocene volcanic basement. This succession has a total thickness of 600–700 m, and reached in average 6–8 km away from its source, with the most distal lava flows reaching 11–12 km. The lavas are aphanitic to micro-porphyritic andesites and dacites (58–67 wt% SiO_2), with a mineral assemblage composed of plagioclase, clinopyroxene, orthopyroxene, Fe–Ti oxides and minor olivine, amphibole and biotite phenocrysts, embedded within an aphanitic groundmass. Two lava samples located to the southeast and east were dated by K–Ar and yielded consistent ages of 1135 ± 17 and 1040 ± 16 ka (Table 2, Fig. 3).

The younger lava flow succession (P–Tb2, Figs. 3 and 4a) forms the upper part of the Basal Tutupaca edifice. It overlies the older succession defining a conspicuous angular discordance. These lava flows crop out at the southern and northwestern flanks of Tutupaca, between 4700 and 4800 and 5350 m asl (Fig. 3) and are 50–100 m thick, viscous lava flows that reach between 3 and 4 km away from the source. The whole lava flow succession has a total thickness of 500 m. They are andesitic and dacitic in composition (60–66 wt% SiO_2) with a porphyritic texture and a mineral assemblage of plagioclase, clinopyroxene, orthopyroxene, Fe–Ti oxides, and minor amphibole and biotite phenocrysts. Two lava flows of this succession were dated by K–Ar at 832 ± 21 and 750 ± 11 ka (Table 2, Fig. 3).

Table 3
Cosmogenic nuclide data (^{10}Be) from boulders of the Azufre debris avalanche deposit. Z is the sample thickness; S is the topographic shielding factor. All the uncertainties reported are 1 sigma.

Sample	UTM Easting	UTM Northing	Elevation (m asl)	Z (cm)	S	^{10}Be[a] (x 10^5 at.g^{-1})	Exposure ages (ka)[b]
TU 2	357153	8114896	5033	3.0	0.994	3.22 ± 0.64	7.8 ± 1.5 (1.6)
TU 3	356499	8115472	5142	4.0	0.968	2.35 ± 0.35	6.0 ± 0.7 (0.7)
TU 5	357083	8114567	4900	4.0	0.982	2.77 ± 0.40	7.3 ± 0.9 (1.0)
TU 6	357400	8114304	4901	5.0	0.98	2.71 ± 0.49	7.3 ± 1.1 (1.2)

[a] Uncertainties reported include the counting statistics. the machine stability (~0.5%) and the blank correction which has a ^{10}Be/^{9}Be ratio of 8.01 ± 0.60 x 10^{-16} for this run.

[b] Uncertainties associated to the ages are 1σ internal uncertainties while 1σ external uncertainties are reported in in parenthesis.

4.1.2. Aligned lava domes

Along the southern flank of Tutupaca, the lava flow successions are cut by at least 15 small domes between 100 and 900 m in diameter, and up to 100 m in height. They were eroded during Pleistocene glaciations. These lava domes (P–Tb3, Fig. 3) are aligned NNW-SSE over a distance of almost 12 km, following the trend of the Western Tutupaca fault. The domes have andesitic and dacitic compositions (60–66 wt% SiO_2) with a mineral assemblage composed of plagioclase, amphibole, biotite and Fe–Ti oxides embedded in a microlitic and slightly vesiculated groundmass. K–Ar ages obtained by Sánchez et al. (1994) and Martínez and Cervantes (2003) for this unit range between 290 ± 27 ka and 240 ± 37 ka. Unfortunately, given the high degree of alteration of the samples, we were unable to obtain a new age for these domes.

4.2. Western Tutupaca edifice

The Western Tutupaca edifice is located at the northwest of Tutupaca, in the prolongation of the Western Tutupaca fault (Figs. 2 and 3). It is a small cone of ~3 km in diameter and 1 km in height, constructed on top of the Basal Tutupaca lava flows at ~4800 m asl, whereas its summit reaches 5800 m asl. The flanks of this edifice have moderate to steep slopes (20°–45°), and were eroded by Pleistocene glaciations, as evidenced by the two generations of moraines at the foot of the cone (P–Mo and H–Mo, Fig. 3), that probably correspond to the Last Glacial Maximum and the Younger Dryas events (see above). Three proximal units have been identified: the basal domes, covered by a succession of lava flows and breccias, and a debris avalanche deposit in its western side. Additionally, we include two pyroclastic deposits that include a large pyroclastic density current deposit (the Callazas unit) and a succession of tephra fallout deposits that crop out to the south of the complex.

4.2.1. Explosive deposits associated with the transition from basal to Western Tutupaca

The Callazas pyroclastic density current deposit crops out between 8 and 12 km to the east and southeast of Tutupaca, on the western bank of the Callazas river (P–Tb4, Fig. 4b). It has an observable thickness of ~5–10 m, and a likely total thickness of several tens of meters. This deposit is made up of 55–60 vol% matrix, 30–40 vol% pumice fragments and <5 vol% lithics. The deposit is massive, structureless and shows abundant degassing pipes (Fig. 4b). The pumiceous bombs are up to 30 cm in diameter, are gray-white in color and have plagioclase, amphibole, biotite, orthopyroxene, and Fe–Ti oxides. Compositional dark to light gray banding is also observed in some pumiceous blocks and bombs. This unit covers the older lava flow succession of the Basal Tutupaca and was covered by the thick moraines ascribed to the Last Glacial Maximum.

A thick (up to 5 m) succession of tephra fallout deposits crops out between 15 and 28 km to the south of Tutupaca. We recognized at least 20–25 pumice-rich, scoria and ash-rich tephra layers of several centimeters to decimeters thick (Fig. 4d). The thickness of individual layers increases to the north and north-east, although no evidence of such layers was found around Tutupaca. Based on geochemical data, at least two pumice-rich layers can be linked with Callazas unit. These tephra layers were eroded during the Last Glacial Maximum. On top of this tephra fallout succession, we collected a peat layer that was dated by radiocarbon at 9980 ± 50 aBP (uncalibrated age). On the basis of these data, we consider that these two units share the same stratigraphic

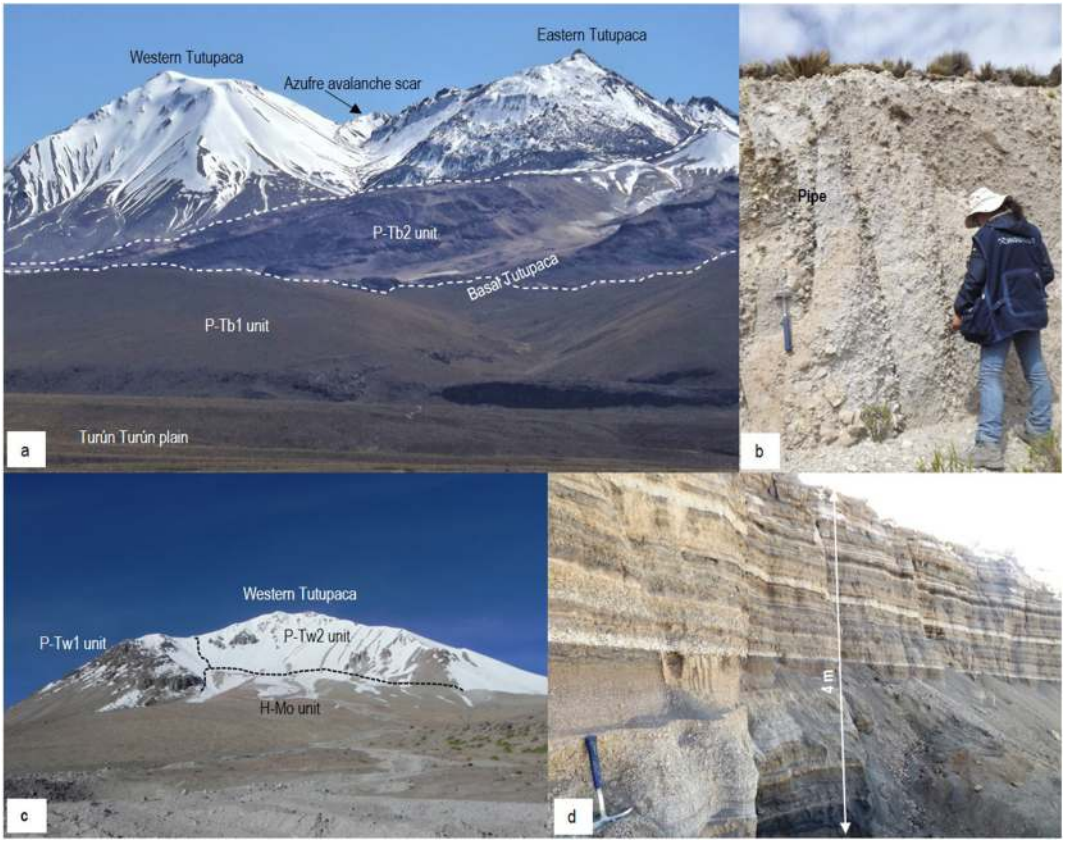

Fig. 4. **(a)** South flank of the Tutupaca volcanic complex showing the angular discordance between the lower (P–Tb1) and upper (P–Tb2) lava successions of the Basal Tutupaca. **(b)** Callazas pyroclastic density current deposit showing subvertical degassing pipe structures. **(c)** Southwest flank of the Western Tutupaca edifice. Domes (P-Tw1) are seen forming the base of the edifice, covered by a succession of lavas and breccias (P-Tw2). **(d)** Succession of tephra fallout deposits outcropping at ~25 km to the south of Western Tutupaca edifice.

position and have a relative age older than the Last Glacial Maximum. In addition, as we show in the subsequent section, some pumice fragments of the tephra fallout succession display the same chemical composition as that of the Callazas event. These deposits are evidence of a succession of large explosive eruptions at the transition between the Basal edifice and Western Tutupaca.

4.2.2. Basal domes

We mapped four lava domes that correspond to the base of the Western Tutupaca edifice (P-Tw1, Fig. 3). They have semicircular basal outlines, with diameters between 1 and 1.5 km, and are up to 500 m high (Figs. 2b, 3 and 4c). The domes have a dacitic composition (64–67 wt% SiO_2) and a mineral assemblage composed of plagioclase, amphibole, biotite, Fe–Ti oxides and traces of titanite and quartz. Dark gray microcrystalline magmatic enclaves (10–20 cm) have also been identified, which have an andesitic composition and contain phenocrysts of plagioclase, amphibole and biotite. One of these domes was dated by K–Ar at 33 ± 5 ka (Table 2), an age that confirms the emplacement of this edifice before the Last Glacial Maximum.

4.2.3. Upper lava flows and breccias

The upper cone of the Western Tutupaca edifice consists of a succession of lava flows and breccias (P-Tw2, Figs. 2b, 3 and 4c). We could not collect samples of this succession because the terrain is very rugged. These lavas and breccias were also affected by intense glacial erosion.

4.2.4. Tacalaya debris avalanche deposit

The Tacalaya debris avalanche deposit outcrops between 4 and 6 km to the west and southwest of the Western Tutupaca edifice, along both sides of the Tacalaya river (P-Tw3, Fig. 3). This deposit is 50–100 m-thick and contains block-rich facies composed of heterogeneous, angular to subangular, centimeter to decimeter lava blocks of andesitic and

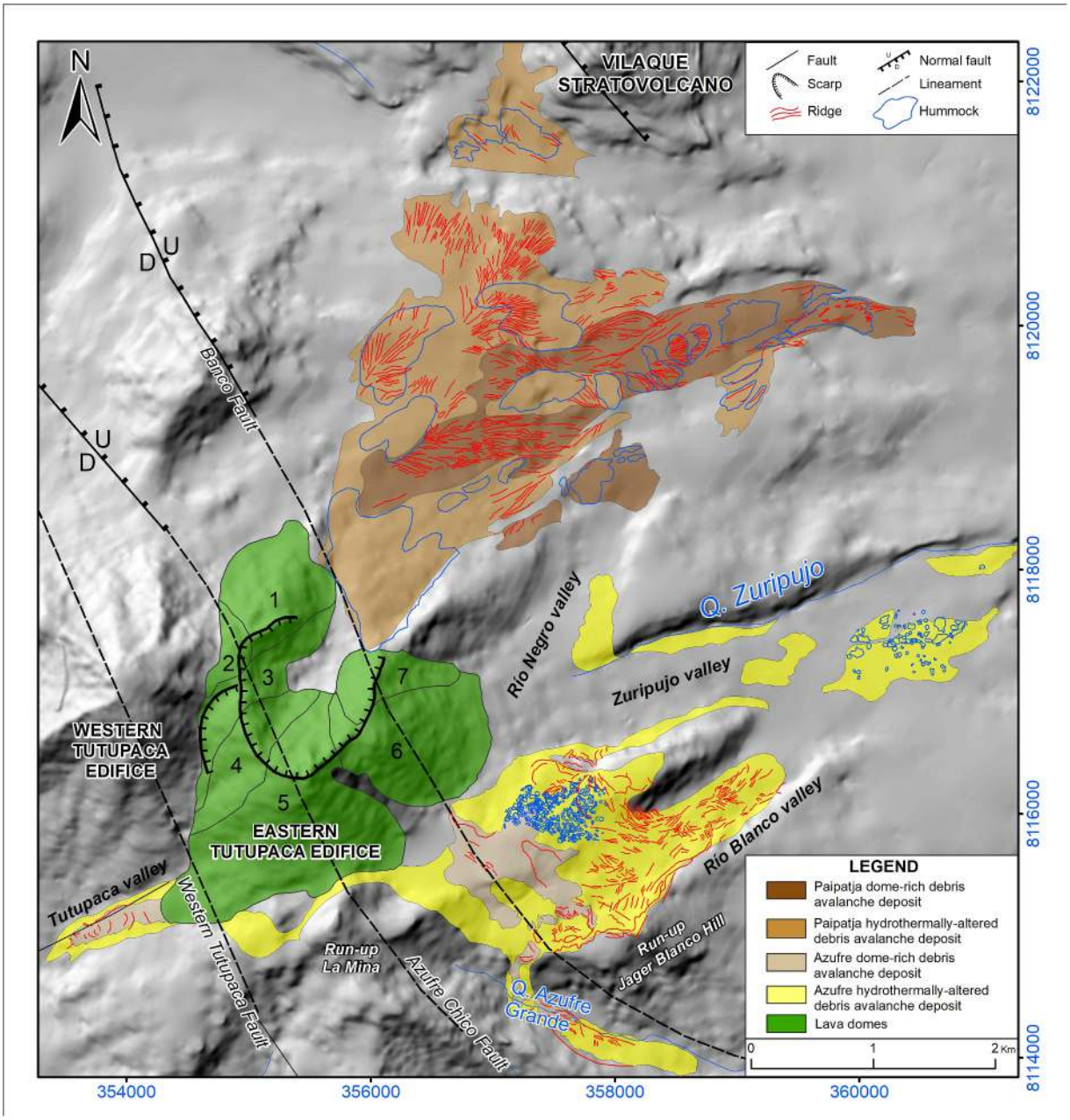

Fig. 5. Simplified geological map showing the debris avalanche deposits concentrated along Eastern Tutupaca volcano (modified from Samaniego et al., 2015; Valderrama, 2016; Mariño et al., 2019).

dacitic compositions (64–67 wt% SiO_2) and a mineral assemblage composed of plagioclase, amphibole, biotite, Fe–Ti oxides and traces of quartz. We also observe (<10 vol%) gray to light-gray breadcrust bombs. Some blocks have typical jigsaw fractures. The deposit's matrix (30–40 vol%) consists of hydrothermally-altered, multicolored (ocher-red to yellow-gray), coarse sand. Based on the mineral assemblage and chemistry, we associate this deposit with the Western Tutupaca edifice. The avalanche deposits are covered by large moraines, probably formed during the Last Glacial Maximum. We correlate these deposits to a scarp identified in the upper flank of the Western Tutupaca edifice, which affected the basal domes and the upper lava flows and breccias of Western Tutupaca. Based on the age of the basal domes and the younger ages of the Last Glacial Maximum periods, we propose that this flank collapse occurred between 33 and 25 ka.

4.3. Eastern Tutupaca edifice

The Eastern Tutupaca edifice is constructed on top of the remnants of the Western and Basal edifices, between 5000 and 5790 m asl. (Figs. 2, 3 and 4a). Eastern Tutupaca is a dome complex made up of seven coalescing lava domes measuring approximately 2.5 km in diameter and ~1 km in height. These domes have been identified from north to south in a counter-clockwise direction (H–Te1, Domes 1 to 7; Figs. 3 and 5). They display homogeneous dacitic compositions (64–66 wt% SiO_2) and a mineral association composed of plagioclase, amphibole, biotite, clinopyroxene, titanite, apatite, quartz and Fe–Ti oxides. The dome complex was affected by two sector collapses, whose conspicuous deposits roughly outcrop towards the east (Azufre debris avalanche) and northeast of the edifice (Paipatja debris avalanche). As a whole, the Eastern Tutupaca edifice is exempt from glacial erosion, suggesting a Holocene age. The main stratigraphic units associated with this edifice are described below.

4.3.1. Azufre debris avalanche deposit

The Azufre debris avalanche deposits mostly crop out to the east of the Eastern Tutupaca edifice (H–Te2a, b; Figs. 3 and 5). These deposits display two different units. The dominant unit corresponds to a massive, unconsolidated, whitish yellow, heterolithic breccia, approximately 30–40 m thick. This deposit is mostly composed of hydrothermally-altered materials (the so-called "hydrothermally-altered unit", Fig. 6b). The block to matrix ratio of this deposit is 40/60 to 30/70 vol%. The blocks present evidence of fracturing and cataclasis. The deposit's matrix consists of fractured, hydrothermally-altered sand-sized material. The blocks are a few centimeters to meters in diameter and are of three types: hydrothermally-altered lavas, aphanitic andesites, and unaltered, amphibole-bearing dacites. Based on the chemical and petrographic characterization (see below), we conclude that the first two correspond to the Basal Tutupaca edifice and the third one is related to the recent domes. The second unit mostly outcrops in the proximal zone (up to 2 km from the source domes). It has a thickness of up to 10–15 m and it covers the hydrothermally-altered unit. The deposit is a block-supported, mono-lithological (predominantly unaltered lave dome blocks), unconsolidated and massive unit (the so-called "dome-rich unit", Fig. 6b). Angular to subangular blocks have maximum diameters of 4–5 m, and display "jigsaw fractures" and prismatically-jointed block structures. This unit is made up of 60–70 vol% of blocks and 40–30 vol% of matrix.

Numerous hummocks have been identified in the Azufre debris avalanche deposit (Figs. 5 and 6c). In the upper part of Cerro Zuripujo, we mapped more than 100, small-sized (10–50 m in diameter, 2–10 m high) hummocks, which are mostly made of fine-grained hydrothermal material, although in the distal lobe of the avalanche there are also examples of block-rich hummocks. In the central part of the deposit, elongated ridge structures were also identified.

Four large boulders (size >2 m) were sampled for cosmogenic nuclide dating (Fig. 5, Table 3). Exposure ages range from 6.0 ± 0.7 to 7.8 ± 1.5 ka (1σ internal). Given that the stratigraphic, and morphological evidences suggest that the Azufre debris avalanche occurred during one single event, the obtained ages should point to a single mean age. This criterion is confirmed statistically as all four ages agree within

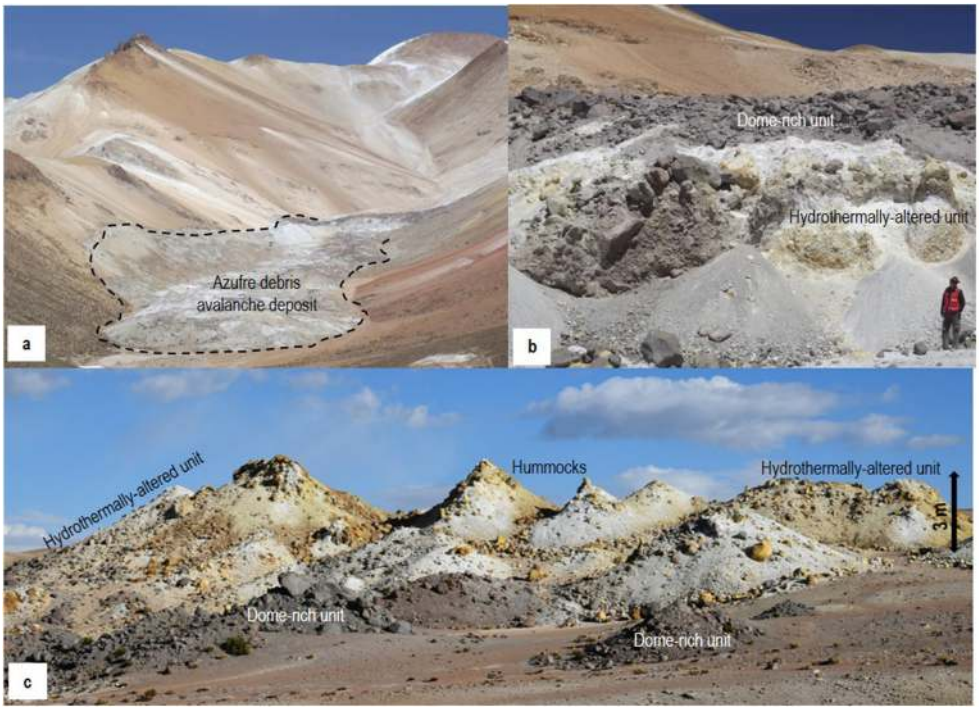

Fig. 6. **(a)** The Azufre debris avalanche deposit in the Azufre ravine. The dotted line marks a run-up on the right bank of the valley. **(b)** Detailed view of the contact between the unit enriched in hydrothermal materials and the domes blocks. **(c)** Hummock field located approximately 4 km away from the source area. They are up to 3–5 m tall (Valderrama, 2016; Mariño et al., 2019).

uncertainty, showing a unimodal distribution (chi-square test = 2.3/7.8; n = 4) with a weighed-mean age of 6.8 ± 0.5 ka. The Mean Standard Weighted Deviation of the distribution equals to 0.8 ka and we derived a 1σ weighted standard deviation of 0.8 ka. The final age obtained for this event is thus 6.8 ± 0.8 ka. The Holocene age of the Azufre debris avalanche is consistent with the lack of glacial erosion of the Eastern Tutupaca edifice.

We associated this debris avalanche deposit with a collapse scar located on the western flank of the Eastern Tutupaca edifice, near the border with Western Tutupaca (Fig. 5). This escarpment affected the older domes (1, 2 and 3 domes), is open to the south-east, and is ~0.6 km-long. The debris avalanche was channeled by the old glacial valleys of the Basal edifice, reaching 7 km in Zuripujo, 3.4 km in Azufre Grande, 2.6 km in Río Blanco, 2.2 km in Tutupaca and 1.1 km in Río Negro ravines. The debris avalanche deposits display two run-ups above the Yager Blanco Hill and in an area called La Mina, where the height of the run-up is 30–125 m from the valley bottom. We also found a remarkable super-elevation feature in the Azufre Grande valley, where the debris avalanche deposits reached 40–45 m above the valley bottom on the left flank (Fig. 6a). These features suggest this debris avalanche had a high mobility and energy (*cf.* Pierson, 1985).

4.3.2. *The historical deposits of the Eastern Tutupaca edifice*

Recent fieldwork identified three volcanic units of historical age, to the east, northeast and north of Eastern Tutupaca. These units are the Zuripujo pyroclastic density current deposits, the Paipatja debris avalanche deposit, and the Paipatja pyroclastic density current deposit (Fig. 3). These deposits were studied in detail by Samaniego et al. (2015), Valderrama et al. (2016), and Mariño et al. (2019). A brief description of these units is presented below.

4.4.2.1. Zuripujo pyroclastic density current deposits. These deposits crop out in the lower part of the Zuripujo valley, 8 and 10 km east of the Eastern Tutupaca edifice (H–Te3, Figs. 3 and 7a, and b). It is a 2 to 5 m-thick unit composed of three block-and-ash flow deposits, with centimeter scale interstratifications of ash-rich layers, showing cross-bedding and laminations (Fig. 7b). The block/matrix ratio of this deposit is of 20/80 to 30/70 vol%. The ash-rich matrix is gray in color, unconsolidated and composed of medium size ash (Fig. 7b). The deposit is mostly polylithologic, but the most common lithology is dark gray, unaltered, dense dacite blocks (65–67 wt% SiO_2) bearing plagioclase, amphibole and biotite in a glass-rich groundmass. Blocks and breadcrust bombs are interpreted as representative of the initial phases of a dome collapse. Three charcoal samples were dated and yielded almost identical ^{14}C ages of 230 ± 30, 220 ± 30 and 190 ± 30 aBP (Samaniego et al., 2015).

4.4.2.2. Paipatja debris avalanche deposits. These deposits crop out to the northeast and north of the Eastern Tutupaca edifice, reaching 6 km from the amphitheater, covering an area of ~12–13 km^2, and a minimum volume of 0.6–0.8 km^3. This deposit is associated with the conspicuous, horseshoe-shaped amphitheater facing the northeast and with a diameter of up to 1 km (Fig. 2b). It displays numerous 20–500 m long elongated ridges, 10–30 m wide, with a coarser core, finer troughs, and less frequent hummocks. Following the interpretation of Valderrama et al. (2016), these structures resulted from particle segregation in granular flows during emplacement of the avalanche. As for the Azufre deposit, two units have been identified, the first that is enriched in hydrothermally-altered lave blocks, and the other that contains relatively unaltered lava dome blocks (H–Te4a, b; Figs. 3 and 5).

The outcrops of the hydrothermally-altered unit are variably colored, yellow, red and brown (Fig. 7c). The deposit consists of several 200–700 m long mega-blocks. These structures are composed of a heterogeneous polymictic breccia, with abundant jigsaw cracks, in a fine-medium sand matrix. Lava blocks are mostly of andesitic composition, yellowish and highly altered, and to a lesser extent dark gray andesites and dacites.

The dome-rich unit deposit outcrop between 3 and 6 km north and northeast from the amphitheater (Figs. 5 and 7d). It consists of abundant, meter-size (up to 3 m in diameter), unaltered, dark gray blocks of dacitic composition that originate from the domes. Similarly, the blocks

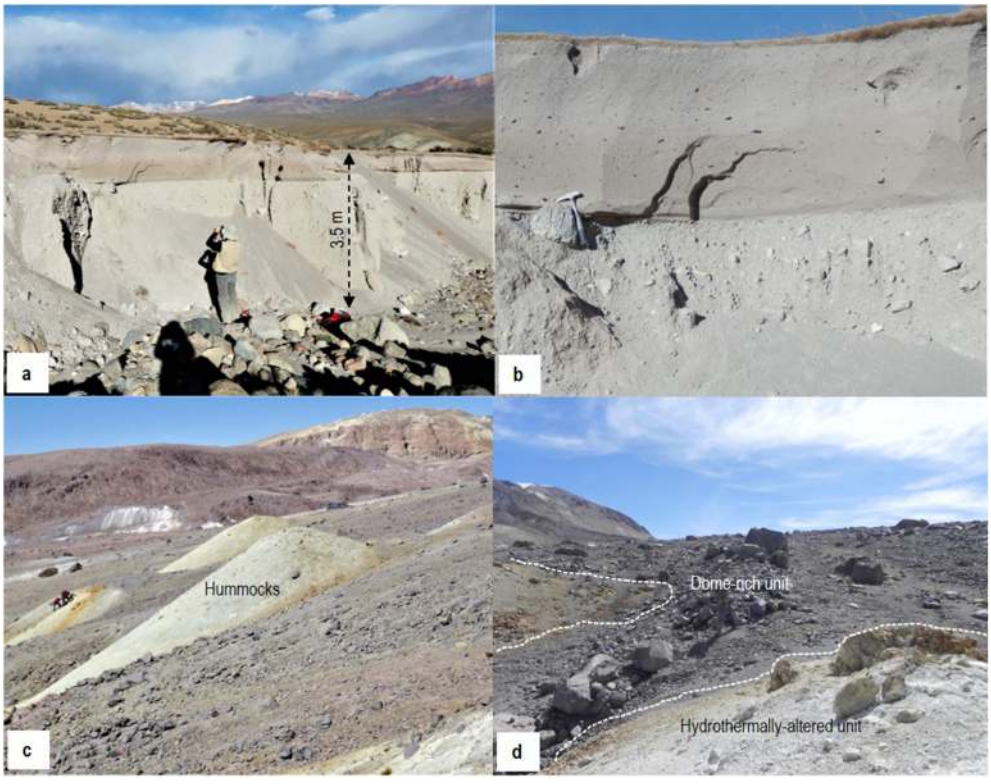

Fig. 7. (a) Zuripujo pyroclastic density current deposit (Z-PDC) in one of the nearby ravines. **(b)** Detail of the Zuripujo deposit covered by the Paipatja pyroclastic density current deposit (hammer for scale). **(c)** Hummocks of metric and decametric dimensions in the hydrothermally-altered unit, in the Paipatja debris avalanche deposits. Area located 3–4 km northeast of the collapse scar. **(d)** Dome-rich unit of the Paipatja debris avalanche deposits. Blocks typically have centimetric to metric dimensions. Sector located between 5 and 6 km northeast of the amphitheater.

show scarce evidence of cataclasis, but abundant prismatic joints. This characteristic suggests that this unit originated from the collapse of a dome, which was still at high temperatures.

4.4.2.3. Paipatja pyroclastic density current deposit. This deposit is located to the east, northeast, and north of the Eastern Tutupaca edifice, reaching 10–12 km away from the vent (H–Te5a, b; Fig. 3). Its thickness varies from 0.5 to 2 m on the plain to 2–5 m in the valleys. In the medial sectors, 4–6 km from the source, the pyroclastic density current deposit is massive, matrix-supported, with 20–40 vol% of blocks. The deposit's top contains abundant bombs, which vary from 10 to 50 cm in size. In the distal areas, from 6 to 12 km (Callazas river and Suches lake), the deposit consists of medium to coarse ash, enriched in bombs at the top. Thus, three types of blocks were identified: the most abundant are dense dacite blocks; followed by less abundant vesicular cauliflower and breadcrust-type bombs, and in a very small proportion there are altered andesites. Two units have been identified in the Paipatja pyroclastic density current deposit: a lower, widespread, bomb-poor facies unit (H-Tr5a), and an upper unit that is bomb-rich (H-Tr5b; Fig. 3).

Samaniego et al. (2015) estimated the volume of this deposit about 6.5–7.5 $\times$ 10^7 m^3. This value together with rough estimates of the ash emitted during this event point to a Volcanic Explosivity Index (VEI) 3 eruption. They also proposed that the Paipatja pyroclastic density current deposits and the Paipatja debris avalanche were associated with an explosive event and flank collapse, that occurred simultaneously. Two ^{14}C dates were reported for the Paypatja pyroclastic density current deposits and yield ages of 235 $\pm$ 35 and 220 $\pm$ 40 aBP, which are identical to the ages obtained at Zuripujo pyroclastic density deposits. These ^{14}C ages correspond to the period 1731 to 1802 CE (Samaniego et al., 2015), which coincides with the two historic eruptions of 1787–89 and 1802 CE, reported by Zamácola y Jaúregui (1804) and Valdivia (1847).

5. Petrologic characteristics

5.1. Petrography

The Basal edifice lavas are porphyritic andesites and dacites (~30 vol % phenocrysts) with a matrix (70 vol%) composed of interstitial glass and microlites (<100 μm) of plagioclase, clinopyroxene, and Fe–Ti oxides. The phenocryst assemblage of Basal edifice samples is composed of plagioclase (<2 mm; 15 vol%), clinopyroxene (<1 mm; 7 vol%), orthopyroxene (<0.5 mm; 3 vol%), amphibole (<0.4 mm; 2 vol%), biotite (<0.5 mm; 2 vol%) and Fe–Ti oxides (~1 vol%). The andesitic lava samples of the P–Tb1 unit also contain scarce olivine (< 0.5 mm) and, include enclaves with acicular plagioclase and clinopyroxene phenocrysts. The petrography of aligned domes is characterized by plagioclase, clinopyroxene, amphibole, biotite, and Fe–Ti oxide phenocrysts, the matrix is slightly vesiculated (5–10 vol%).

Pumice fragments of the transitional Callazas pyroclastic density current unit show a mineral assemblage composed of plagioclase (7 vol %), amphibole (5 vol%), biotite (3 vol%), clinopyroxene (2 vol%) and Fe–Ti oxides (~1 vol%). This mineral assemblage, characterized by the ubiquitous presence of amphibole and biotite is in stark contrast with that observed in Basal Tutupaca samples. It is worth noting that some pumice fragments have a light and dark banded texture, suggesting a magma mixing process between dacitic and andesitic magmas.

Samples from Western and Eastern Tutupaca are porphyritic (~35 vol%) and partially vesiculated (~5 vol%) dacites with phenocrysts of plagioclase (< 2 mm; 15–20 vol%), amphibole (< 0.8 mm; 10–15 vol%), biotite (< 0.5 mm; 3–5 vol%), clinopyroxene (< 0.4 mm; 2–3 vol%), and Fe–Ti oxides, with titanite, apatite and quartz as accessory phases (<1–2 vol%). The matrix is composed of interstitial glass and plagioclase, amphibole, and Fe–Ti oxide microlites. The breadcrust-type bombs of the Paipatja pyroclastic density current unit are vesiculated (~15 vol%), have porphyritic textures (~15–20 vol% phenocrysts) and an identical mineral assemblage to the dense blocks. In some dome blocks of the Western and Eastern edifices, scarce mafic magmatic enclaves that are fine-grained and rounded (2–10 cm in diameter) are present, with a quenched groundmass of randomly oriented, interlocking, elongate, or acicular crystals of plagioclase, amphibole and biotite (Manrique et al., 2020). The amphibole, biotite and titanite show rims of Fe–Ti oxide and pyroxene microlites. In Western and Eastern Tutupaca, we observe scarce quartz phenocrysts that are subhedral to anhedral and frequently display resorption textures. The phenocrysts from the Eastern Tutupaca samples show common disequilibrium textures such as reverse zonation, resorption zones and overgrowth rims.

5.2. Whole-rock major and trace elements

Basal, Western and Eastern Tutupaca samples define a high-K calc-alkaline magmatic trend, that spans from andesites to dacites (58.3–69.4 wt% SiO_2) for Basal Tutupaca, and mostly dacites (63.0–68.0 wt% SiO_2) for Western and Eastern Tutupaca (Fig. 8, Table 3). The enclaves found in the Western and Eastern edifices display basaltic andesitic to andesitic compositions (52.5–57.2 wt% SiO_2). In general, major oxides (except K_2O) are negatively correlated with silica content. The light gray pumices of the Callazas pyroclastic density current unit and some samples from the distal tephra fallout deposits have the highest silica contents (65.7–69.4 wt% SiO_2; 4.0–4.6 wt% K_2O), while the gray vesiculated pumice of the Callazas unit have andesitic compositions (60.0–60.3 wt% SiO_2; 2.6–2.8 wt% K_2O). We observe that the gray pumices of the Callazas unit display a slight scattering, associated with the magma mixing process observed in these samples. The pumice in Paipatja pyroclastic density current deposits show a slight increase in silica (67–68 wt% SiO_2; 3.5–3.9 wt% K_2O).

For most major elements, the Western and Eastern Tutupaca samples lie on the trend defined by the Basal Tutupaca edifice. The overall magmatic trend is characterized by negative correlations between silica and Sr, Y, some transition metals (e.g., Cr, Ni, V), and the heavy rare-earth elements (HREE, e.g. Dy, Yb), however, some samples show a slight scattered trend in Yb, Cr, Ni, and Dy. Conversely, the large ion lithophile elements (LILE, e.g., Rb, Th) display a positive correlation with silica content (Fig. 8), however, the samples of tephra fallout deposits of Western Tutupaca have a slight scattered trend. Some medium rare-earth elements (MREE, e.g., Sm, Gd), HREE (e.g., Er) and high-field-strength elements (HFSE e.g., Zr) have very scattered trends. The dacitic pumice of the Callazas unit displays an enrichment in LILE (e.g., Rb) and a notable depletion in the Sr, which results in high Rb/Sr ratios compared to the other samples of the complex that show a single trend. The Eastern edifice samples show a slight enrichment in LREE (e.g., La) and Sr and a notable depletion in the MREE (e.g. Dy) and HREE (e.g. Yb), which results in high La/Yb ratios (41–83) and Dy/Yb ratios (2.5–3.4) compared to those for the whole Tutupaca volcanic complex. The gray pumices of the Callazas PDC unit and two samples of the tephra fallout deposits of Western Tutupaca have low La/Yb ratios (32.2–20.8) and Dy/Yb ratios (1.8–2.3). In the SiO_2 *versus* La/Yb and Dy/Yb diagrams (Fig. 8), we observe that the Western and Basal Tutupaca samples define a broad flat trend, whereas the Eastern Tutupaca samples display a different grouping with high REE ratios. This characteristic could be associated with deep-seated processes in the lower crust involving assimilation and fractional crystallization of garnet and/or amphibole (*cf.* Mamani et al., 2010; Rivera et al., 2014; Blum-Oeste and Wörner, 2016).

6. Discussion

6.1. Development of Tutupaca volcanic complex

Based on the stratigraphic, geochronological and geochemical data (Table 4), we propose that Tutupaca is a volcanic complex with a long-

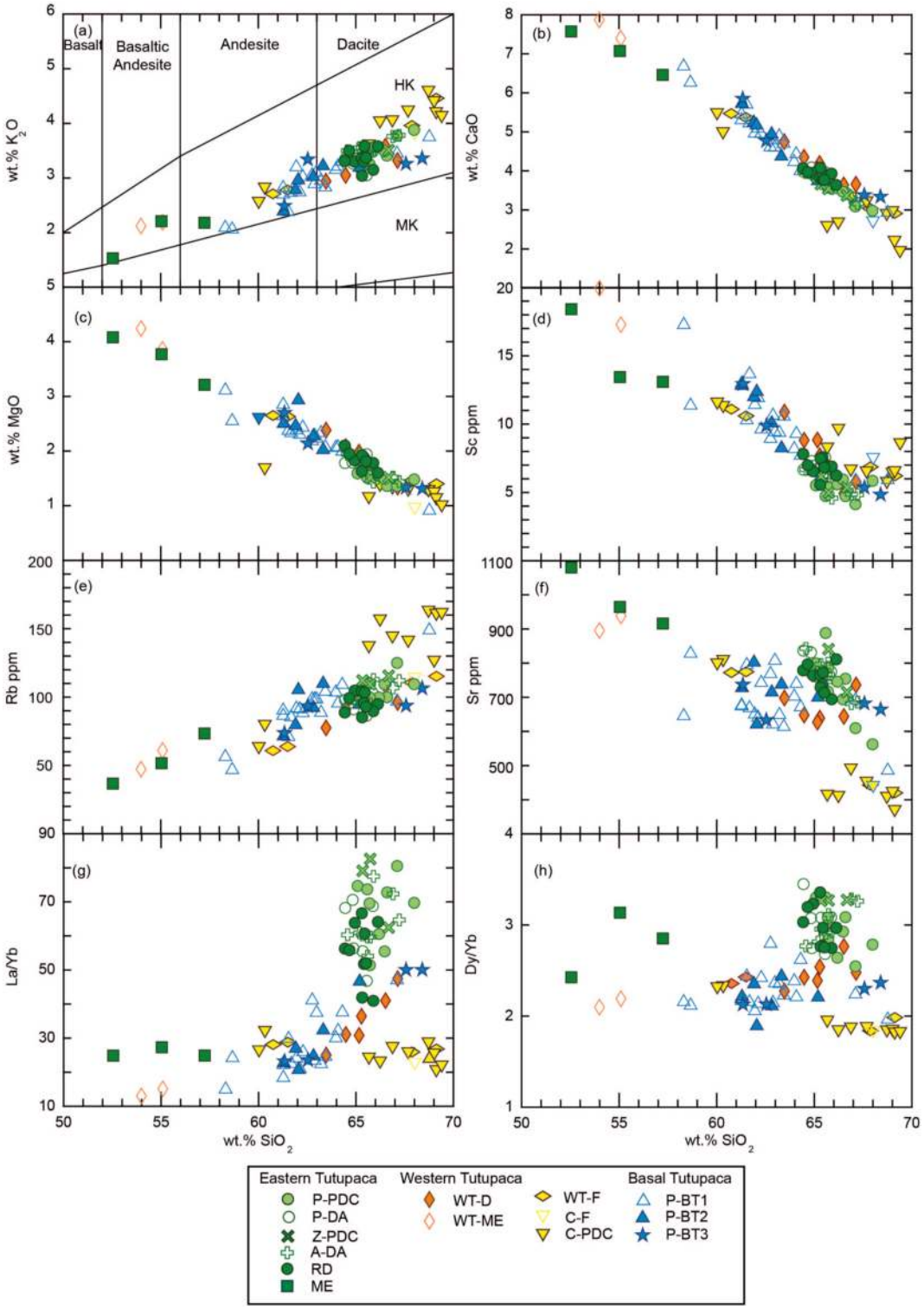

Fig. 8. Major **(a–c)** and trace element concentrations **(d–f)** and ratios **(g–h)** for eruptive products of the Tutupaca, plotted versus SiO_2 as a differentiation index. Subdivision in K_2O versus SiO_2 diagram is from Peccerillo and Taylor (1976). MK, medium potassium; HK, high potassium; P-PDC, Paipatja pyroclastic density currents deposits; P-DA, Paipatja debris avalanche deposits; Z-PDC, Zuripujo pyroclastic density currents deposits; A-DA, Azufre debris avalanche deposits; RD, recent domes; ME, mafic enclaves; WT-D, Western Tutupaca domes; WT-ME, Western Tutupaca mafic enclaves; WT-F, Transitional Basal to Western Tutupaca tephra fallout deposits, C–F, Callazas tephra fallout deposit; C-PDC, Callazas pyroclastic density currents deposits; P-BT1, Basal Tutupaca lava flows; P-BT2, Basal Tutupaca lava flows; P-BT3, aligned domes.

lasting evolution covering at least 1 Ma. The Basal Tutupaca developed from 1150 to 1025 ka to 800–750 ka and was mostly characterized by effusive activity corresponding to two lava flow successions separated by a conspicuous angular unconformity. This unconformity suggests that a significant time gap (with the subsequent erosion) separated the two lava flow successions. The lava pile was intruded around 300–200 ka by at least 15 dacitic domes aligned along the NW-SE trending Western Tutupaca fault. The Basal edifice is highly eroded by Pleistocene

Table 4
Generalized stratigraphy showing the main eruptive stages at Tutupaca volcanic complex.

Edifice	Units	Age	Magma composition
Eastern Tutupaca	Paipatja pyroclast density current deposits: Bomb-poor unit (H–Te5a) and bomb-rich unit (H–Te5b) Paipatja debris avalanche deposit: Hydrothermally-altered unit (H–Te4a) and Dome-rich unit (H–Te4b)	218 ± 14 aBP	Amphibole and biotite-bearing dacites (65–68 wt% SiO_2)
	Zuripujo pyroclast density current deposit (H–Te3)		Amphibole and biotite-bearing dacites (65–68 wt% SiO_2)
	Azufre debris avalanche deposit: Hydrothermally-altered unit (H–Te2a) and Dome-rich unit (H–Te2b)	6-7.5 ka	
	Lava domes (D1-7) (H–Te1)		Amphibole and biotite-bearing dacites (64–66 wt% SiO_2) + andesitic enclaves (52–57 wt% SiO_2)
	Pleistocene-Holocene moraines (H–Mo) associated with teh Younger Dryas event (YD)	10-12 ka	
	Pleistocene morraines (P–Mo) associated with the Last Glatial maximum (LGM)	17-25 ka	
Western Tutupaca	Tacalaya debris avalanche deposit (P-Tw3)		Amphibole and biotite-bearing dacites (64–67 wt% SiO_2)
	Upper lava flow successions (P-Tw2)		
	Basal domes (P-Tw1)	30-35 ka	Amphibole and biotite-bearing dacites (64–67 wt% SiO_2) + andesitic enclaves (54–55 wt% SiO_2)
	Callazas pyroclastic density current deposit and associated tephra fallout deposits (P-Tw0)		Amphibole-bearing andesites (60–61 wt% SiO_2) and dacites (66–69 wt% SiO_2)
Basal Tutupaca	Aligned lava domes (P–Tb3)	200-300 ka	Amphibole-bearing andesites and dacites (60–66 wt% SiO_2)
	Younger lava flow successions (P–Tb2)	750-850 ka	Two-pyroxene andesites and dacites (61–65 wt% SiO_2)
	Older lava flow successions (P–Tb1)	1025-1150 ka	Two-pyroxene andesites and dacites (58–69 wt% SiO_2)

glaciations that are responsible for the formation of the radial glacial valleys around its summit. In addition, this edifice displays widespread hydrothermal activity, especially in the summit and its upper flanks. The hydrothermal system responsible for such surface manifestations is still active as it is shown by the several hot-springs around the edifice.

The transition towards the younger edifices is marked by a period characterized by frequent explosive eruptions, as shown by the tephra fallout deposits to the SW of the edifice. The most important eruption in this transitional period generated a large pyroclastic density current and tephra fallout deposits (Callazas unit), associated with magmas with the highest silica content of the Tutupaca magmatic series. This explosive phase occurred before the Last Glacial Maximum.

Western Tutupaca was constructed on the remnants of the Basal edifice and developed since 30–35 ka in the northern part of the complex. It is located in the northern prolongation of the NW-SE trending faults. This edifice was characterized by the formation of several dacitic lava domes, and suffered a flank collapse, whose deposits filled the Tacalaya river. Western Tutupaca was also affected by Pleistocene glacial erosion and is partially covered by large moraines, probably associated with the Last Glacial Maximum, between 25 and 17 ka. Based on stratigraphic evidence, the Tacalaya sector collapse occurred before this time.

Eastern Tutupaca was constructed on top of the hydrothermally-altered Basal edifice, to the east of Western Tutupaca (Fig. 9a). It is a dacitic dome complex unaffected by the Pleistocene glaciations, suggesting a Holocene age. The older domes (D1-3), located in the northern part of the complex (Fig. 9b), were affected by a sector collapse that triggered the Azufre debris avalanche. This deposit was dated at 6–7.5 ka. Inside this amphitheater, volcanic activity reconstructed the dome complex with the successive extrusion of domes (D4-7, Fig. 9c). This newly reconstructed Eastern Tutupaca edifice was affected by a second sector collapse that formed the current amphitheater, the Paipatja deposit and pyroclastic successions that spread-out to the NE of the edifice (Fig. 9d). This second sector collapse occurred historically at 218 ± 14 aBP (Samaniego et al., 2015).

6.2. Successive destabilization of a dacitic dome complex

The successive sector collapse events affecting the Eastern Tutupaca edifice formed two debris avalanche deposits that display some key characteristics, such as the presence of two distinct facies: a widespread hydrothermally-altered facies composed of materials from the Basal edifice; and, a dome-rich facies with material from the recent domes. Although the proportion of these two facies is not the same, the presence of these two units shows that a similar mechanism could be invoked. As mentioned by Samaniego et al. (2015) and Valderrama et al. (2016) for the Paipatja debris avalanche event, an enhanced dome-growth process together with the fact that these domes were constructed on top of a highly hydrothermally-altered edifice induced the sector collapse of the dome complex and of the upper part of the Basal edifice. This model can also be applied to the older Azufre sector collapse, although some differences exist between both events, namely the fact that the Paipatja sector collapse was accompanied by an explosive eruption, whereas no explosive events have been identified related to the Azufre sector collapse. However, as mentioned earlier, the presence of prismatically-jointed blocks in the debris avalanche deposits suggests that in both cases, the domes were still hot at the time of collapse. Thus, it seems highly plausible that both debris avalanches could have been caused by the loading of the new lava domes on the altered Basal edifice, together with the increasing pore fluid pressure due to the reactivating hydrothermal system.

6.3. Hazard assessment

Based on the reconstruction of the eruptive chronology of this volcanic center, a future eruption of the Eastern Tutupaca volcano could be characterized by the formation of a dacitic dome and related formation of block-and-ash pyroclastic density currents associated with sector collapse. In the case of an enhanced dome growth phase, the formation of a large lava dome on the present amphitheater is a plausible situation. Such a scenario would be similar to the last eruption of Tutupaca that occurred between the 18th and 19th century. This scenario implies the occurrence of a sector collapse of the newly formed dome complex, which can be accompanied by a large explosive phase. The potential occurrence of a large eruption is supported by the fact that Eastern Tutupaca experienced at least two sector collapses during the last millennia. However, we consider that a large eruption scenario is a less probable event in comparison to smaller dome-forming eruptions. In addition, during the rainy season (from December to March), frequent lahars would affect the ravines around the volcano. These scenarios have been considered in the recently published volcanic hazard map for

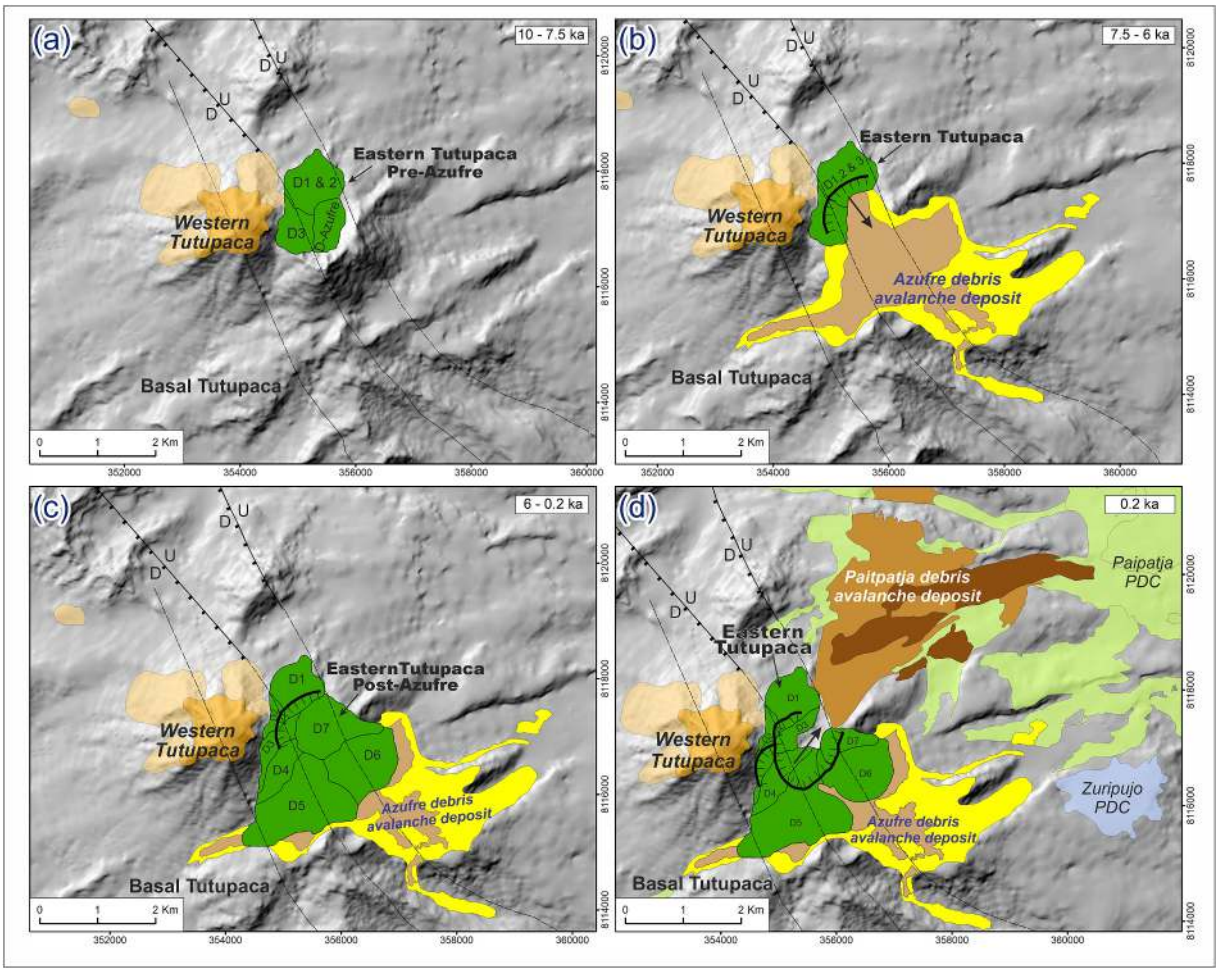

Fig. 9. Sketch diagrams showing the evolution of Eastern Tutupaca edifice before and after the two sector collapses.

Tutupaca (Mariño et al., 2019).

During the past eruptions of Eastern Tutupaca, the eruptive products affected uninhabited areas of the high Peruvian Andes, and tephra fallout had only a minor regional impact. However, if a large eruption were to occur, it could affect a much larger population of at least ten thousand inhabitants living within a 25 km radius of the volcano, including people in the Huaytire, Candarave, Cairani, Huanuara and Tumilaca villages. Furthermore, important mining projects, such as Cuajone, Toquepala and Quellaveco, are vulnerable. In addition, the area around Tutupaca volcano is the main source of water for agriculture and mining, which could both be affected during an eruption.

7. Conclusions

The Tutupaca volcanic complex (17°01′ S, 70°21′ W) is composed of an old, hydrothermally altered and highly eroded Basal edifice, and younger twin peaks, Western and Eastern Tutupaca, located in the northern part of the complex. The Basal edifice is mostly composed of a first lava flow succession up to 500 m in thickness, dated at 1150–1025 ka, followed by a second lava flow succession between 850–750 ka. This edifice was then intruded by a series of domes aligned domes in NNW-SSE direction. The lava flows and the aligned domes are andesitic to dacitic (58.7–69.6 wt% SiO_2), and they contain a mineral assemblage composed of plagioclase, clinopyroxene, amphibole, biotite, Fe–Ti oxides, and olivine as an accessory mineral. We note that the upper part of the Basal edifice displays pervasive hydrothermal alteration.

After a period of large explosive eruptions that marked the transition from Basal to younger edifices, the Western Tutupaca was constructed on the remnants of the basal volcano. This edifice is composed of a series of dacitic lava domes dated at 30–35 ka, and suffered a flank collapse whose deposits outcrop in the Tacalaya river valley. This edifice was highly eroded by the Pleistocene glaciations. Lastly, the youngest Eastern edifice is composed of at least seven coalescing lava domes and associated block-and-ash flow and debris avalanche deposits. All samples from Eastern Tutupaca have dacitic compositions (64.4–68.0 wt% SiO_2) and display a mineral assemblage composed of plagioclase, amphibole, clinopyroxene, biotite and Fe–Ti oxides, with some changes through time.

We identified two debris avalanche deposits associated with Eastern Tutupaca. An older unit (Azufre debris avalanche deposit) that was channeled in the valleys located to the east and southeast of the Basal edifice, reaching up to 3.5 km from the source region. The age of this avalanche was constrained by four cosmogenic nuclide exposure dates on boulders (^{10}Be/feldspar) providing a weighted-mean age of 6.8 ± 0.8 ka. The younger unit (Paipatja debris avalanche deposit) outcrops immediately to the northeast of the amphitheater and was associated with a large pyroclastic density current deposit that was radiocarbon dated at 218 ± 14 aBP (Samaniego et al., 2015). Both debris avalanche deposits have two different units: (1) the main hydrothermally-altered debris avalanche deposit, that is a whitish-yellow volcanic breccia with heterolithic and heterometric blocks, containing material from the Basal and the Eastern Tutupaca edifices; and (2) the dome-rich debris avalanche deposit, composed of non-altered dome blocks from Eastern Tutupaca. In proximal areas, the dome-rich unit overlaps the hydrothermally-altered unit; whereas, in distal areas, these two units are mixed forming a hummocky and/or ridged topography. In addition to

the similar facies of these deposits, we suggest that the triggering mechanism for these debris avalanches was similar. We propose that both sector collapses were triggered by the loading of the dacitic lava domes on the altered Basal edifice, together with the increasing pore fluid pressure due to the reactivating hydrothermal system.

Author statement

J. Mariño: Conceptualization, Methodology, Investigation, Writing – original draft, Writing – review & editing, P. Samaniego: Conceptualization, Methodology, Investigation, Writing – original draft, Writing – review & editing, Funding acquisition, N. Manrique: Investigation, Writing – review & editing, P. Valderrama: Investigation, Writing – review & editing, O. Roche: Investigation, Writing – review & editing, B. van Wyk des Vries: Investigation, Writing – review & editing, H. Guillou: Investigation, Writing – review & editing, S. Zerathe: Investigation, Writing – review & editing, C. Arias: Investigation, C. Liorzou: Investigation

Declaration of competing interest

The authors declare that they have no known competing financial interests or personal relationships that could have appeared to influence the work reported in this paper.

Acknowledgements

This work is part of a Peruvian-French cooperation programme carried out between the Instituto Geológico, Minero y Metalúrgico (INGEMMET, Peru), and the Institut de Recherche pour le Développement (IRD, France) through a "Jeune Equipe Associée à l'IRD" (JEAI) project. PV and NM thank IRD for financial support through the ARTS and BEST scholarship programs. We would thank Swetha Venegopal and Will Kochtitzky for english improvement of a previous version of this manuscript. The sample processing and chemical extraction of the ^{10}Be were performed at the GTC plateform (ISTerre, Grenoble). We gratefully thank Francis Coeur for the sample processing. The ^{10}Be measurements were performed at the ASTER AMS national facility (CEREGE, Aix-en-Provence) which is supported by the INSU/CNRS, the ANR through the "Projets thématiques d'excellence" program for the "Equipements d'excellence" ASTER-CEREGE action and IRD. This research was partially financed by the French Government Laboratory of Excellence initiative n°ANR-10-LABX-0006, the Région Auvergne and the European Regional Development Fund. This is Laboratory of Excellence ClerVolc contribution number 462.

Appendix A. Supplementary data

Last page of the pdf.

References

Adams, N.K., de Silva, S.L., Self, S., Salas, G., Schubring, S., Permenter, J.L., Arbesman, K., 2001. The physical volcanology of the 1600 eruption of Huaynaputina, southern Peru. Bull. Volcanol. 62, 493–518.

Alcalá-Reygosa, J., Palacios, D., Vázquez-Selem, L., 2017. A preliminary investigation of the timing of the local last glacial maximum and deglaciation on Hualca-Hualca volcano - patapampa Altiplano (arid Central Andes, Peru). Quat. Int. 449, 149–160.

Alley, R.B., 2000. The Younger Dryas cold interval as viewed from central Greenland. Quat. Sci. Rev. 19, 213–226.

Arnold, M., Aumaître, G., Bourlès, D.L., Keddaddouche, K., Braucher, R., Finkel, R.C., Nottoli, E., Benedetti, L., Merchel, S., 2013. The French accelerator mass spectrometry facility ASTER after 4 years: status and recent developments on 36Cl and 129I. Nucl. Instrum. Methods Phys. Res. Sect. B Beam Interact. Mater. Atoms 294, 24–28.

Arnold, M., Merchel, S., Bourlès, D.L., Braucher, R., Benedetti, L., Finkel, R.C., Aumaître, G., Gottdang, A., Klein, M., 2010. The French accelerator mass spectrometry facility ASTER: improved performance and developments. Nucl. Instrum. Methods Phys. Res. Sect. B Beam Interact. Mater. Atoms 268, 1954–1959.

Benavente, C., Carlotto, V., del Castillo, B., 2010. Extensión en el arco volcánico actual del Sur de Perú. XV Congreso Peruano de Geología, extended abstracts. Sociedad Geológica del Perú, Pub. Esp 9, 766–769.

Bernard, K., van Wyk de Vries, B., Thouret, J.C., 2019. Fault textures in volcanic debris-avalanche deposits and trans formations into lahars: the Pichu Pichu thrust lobes in south Peru compared to worldwide avalanche deposits. J. Volcanol. Geoth. Res. 371, 116–136.

Blum-Oeste, M., Wörner, G., 2016. Central Andean magmatism can be constrained by three ubiquitous end-members. Terra. Nova 28, 434–440.

Braucher, R., Guillou, V., Bourlès, D.L., Arnold, M., Aumaître, G., Keddadouche, K., Nottoli, E., 2015. Preparation of ASTER in-house 10Be/9Be standard solutions. Nucl. Instrum. Methods Phys. Res. Sect. B Beam Interact. Mater. Atoms 361, 335–340.

Bromley, G.R.M., Schaefer, J.M., Winckler, G., Hall, B.L., Todd, C.E., Rademaker, K.M., 2009. Relative timing of last glacial maximum and late-glacial events in the central tropical Andes. Quat. Sci. Rev. 28, 2514–2526.

Bromley, G., Thouret, J.C., Schimmelpfennig, I., Mariño, J., Valdivia, V., Rademaker, K., Vivanco, S., 2019. In situ cosmogenic 3He and 36Cl and radiocarbon dating of volcanic deposits refine the Pleistocene and Holocene eruption chronology of SW Peru. Bull. Volcanol. 81, 64.

Clavero, J.E., Sparks, R.S.J., Huppert, H.E., Dade, W.B., 2002. Geological constraints on the emplacement mechanism of the Parinacota debris avalanche, northern Chile. Bull. Volcanol. 64, 40–54.

Clapperton, C.M., 1991. Glacier fluctuations of the last glacial - interglacial cycle in the Andes of South America. Bamb. Geogr. Schriften 11, 183–207.

Cobeñas, G., Thouret, J.-C., Bonadonna, C., Boivin, P., 2012. The c. 2030 yr BP Plinian eruption of El Misti volcano, Peru: eruption dynamics and hazard implications. J. Volcanol. Geoth. Res. 241–242, 105–120.

Cotten, J., Le Dez, A., Bau, M., Caroff, M., Maury, R.C., Dulski, P., Fourcade, S., Bohn, M., Brousse, R., 1995. Origin of anomalous rare-earth element and Yttrium enrichments in subaerial exposed basalts: evidence from French Polynesia. Chem. Geol. 119, 115–138.

Cruz, V., Matsuda, K., 2015. Geochemical study of thermal waters in the Tutupaca geothermal zone, tacna, south of Peru. In: Proceedings World Geothermal Congress, 19-25 April 2015, Melbourne, Australia.

de Silva, S.L., Francis, P., 1991. Volcanoes of the Central Andes. Springer, Berlin Heidelberg New York, p. 216.

de La Cruz, N., de la Cruz, O., 2000. Mapa geológico del cuadrángulo de Tarata, a escala 1/50000. INGEMMET.

Detienne, M., 2016. Unravelling the Role of Hydrothermal Alteration in Volcanic Flank and Sector Collapses Using Combined Mineralogical, Experimental, and Numerical Modelling Studies. PhD thesis. Université catholique de Louvain, p. 307.

Donnadieu, F., Merle, O., 1998. Experiments on the indentation process during cryptodome intrusions: new insights into Mount St. Helens deformation. Geology 26, 79–82.

Fidel, L., Zavala, B., 2001. Mapa preliminar de amenaza volcánica del volcán Tutupaca. Boletín 24, Serie C. Geodinámica e Ingeniería Geológica, INGEMMET, p. 109.

Guillou, H., Nomade, S., Carracedo, J.C., Kissel, C., Laj, C., Perez Torrado, F.J., Wandres, C., 2011. Effectiveness of combined unspiked K-Ar and 40Ar/39Ar dating methods in the 14C age range. Quat. Geochronol. 6, 530–538.

Harpel, C., de Silva, S., Salas, G., 2011. The 2 ka eruption of Misti volcano, southern Peru- the most recent Plinian eruption of Arequipa's iconic volcano. Geol. Soc. Am. Spec. Pap. 484, 72.

Hoblitt, R.P., Miller, C.D., Vallance, J.W., 1981. Origin and Stratigraphy of the Deposit Produced by the May 18 Directed Blast. USGS Prof, pp. 401–420. Paper 1250.

Kelfoun, K., Druitt, T.H., van Wyk de Vries, B., Guilbaud, M.N., 2008. Topographic reflection of the Socompa debris avalanche, Chile. Bull. Volcanol. 70, 1169–1187.

Lagmay, A.M.F., van Wyk de Vries, Kerle, N., Pyle, D.M., 2000. Volcano instability induced by strike-slip faulting. Bull. Volcanol. 62, 331–346.

Legros, F., Cantagrel, J.M., Devouard, B., 2000. Pseudotachylyte (frictionite) at the base of the Arequipa volcanic landslide deposit (Peru): implications for emplacement mechanisms. J. Geol. 108, 601–611.

Lifton, N., 2016. Implications of two Holocene time-dependent geomagnetic models for cosmogenic nuclide production rate scaling. Earth Planet Sci. Lett. 433, 257–268.

Lifton, N., Sato, T., Dunai, T.J., 2014. Scaling in situ cosmogenic nuclide production rates using analytical approximations to atmospheric cosmic-ray fluxes. Earth Planet Sci. Lett. 386, 149–160. https://doi.org/10.1016/j.epsl.2013.10.052.

Mamani, M., Worner, G., Sempere, T., 2010. Geochemical variations in igneous rocks of the Central Andean orocline (13°Sto18°S): tracing crustal thickening and magma generation through time and space. Geol. Soc. Am. Bull. 122, 162–182.

Manrique, N., Samaniego, P., Médard, E., Schiavi, F., Mariño, J., Liorzou, C., 2020. Pre-eruptive magmatic processes associated with the historical (218 ±14 aBP) explosive eruption of Tutupaca volcano (southern Peru). Bull. Volcanol. 82, 6.

Mariño, J., Samaniego, P., Manrique, N., Valderrama, P., Macedo, L., 2019. Geología y mapa del Complejo Volcánico Tutupaca. INGEMMET, Boletín, Serie C: Geodin. Ing. Geol. 66, 165.

Martin, L.C.P., Blard, P.H., Balco, G., Lavé, J., Delunel, R., Lifton, N., Laurent, V., 2017. The CREp program and the ICE-D production rate calibration database: a fully parameterizable and updated online tool to compute cosmic-ray exposure ages. Quat. Geochronol. 38, 25–49 quageo.2016.11.006.

Martínez, W., Cervantes, J., 2003. Rocas ígneas en el sur del Perú: nuevos datos geocronométricos, geoquímicos y estructurales entre los paralelos 16° y 18°30' Latitud Sur. INGEMMET, Boletín, Ser. D: Estudios Region. 26, 140.

Peccerillo, P., Taylor, S.R., 1976. Geochemistry of Eocene calc-alkaline volcanic rocks from the Kastamonu area. Northern Turkey. Contrib. Mineral. Petrol. 58, 63–81.

Pierson, T.C., 1985. Initiation and Flow Behavior of the 1980 Pine Creek and Muddy River Lahars, Mount St. Helens, Washington, vol. 96. Geological Society of America Bulletin, pp. 1056–1069.
Quang, C.X., Clark, A.H., Lee, J.K.W., Hawkes, N., 2005. Response of supergene processes to episodic Cenozoic uplift, pediment erosion, and ignimbrite eruption in the Porphyry Copper Province of southern Perú. Econ. Geol. 100, 87–114.
Reid, M.E., Sisson, T.W., Brien, D.L., 2001. Volcano collapse promoted by hydrothermal alteration and edifice shape. Mount Rainier, Washington. Geology 29, 779–782.
Richards, J.P., Villeneuve, M., 2001. The Llullaico volcao, northwest Argentina: construction by pleistocene volcanism and destruction by sector collapse. J. Volcanol. Geoth. Res. 198, 19–34.
Rivera, M., Thouret, J.C., Samaniego, P., Le Pennec, J.L., 2014. The 2006–2009 activity of Ubinas volcano (Peru): petrology of the 2006 eruptive products and insights into genesis of andesite magmas, magma recharge and plumbing system. J. Volcanol. Geoth. Res. 270, 122–141.
Rivera, M., Samaniego, P., Vela, J., Le Pennec, J.L., Guillou, H., Paquette, J.L., Liorzou, C., 2020. The eruptive chronology of the Yucamane-Calientes compound volcano: a potentially active edifice of the Central Andes (southern Peru). J. Volcanol. Geoth. Res. 393, 106787.
Samaniego, P., Valderrama, P., Mariño, J., van Wyk de Vries, B., Roche, O., Manrique, N., Malnati, J., 2015. The historical (2018±14 aBP) explosive eruption of Tutupaca volcano (Southern Peru). Bull. Volcanol. 77, 1–18.
Samaniego, P., Rivera, M., Mariño, J., Guillou, H., Liorzou, C., Zerathe, S., Delgado, R., Valderrama, P., 2016. The eruptive chronology of the Ampato-Sabancaya volcanic complex (Southern Peru). J. Volcanol. Geoth. Res. 323, 110–128.
Sánchez, A., de la Cruz, N., Quispesivana, L., Rodriguez, W., López, J.C., Enriquez, J., Mongue, R., Quispesivana, W., Imaña, E., León, W., Guzmán, A., Olivares, P., Morche, W., Aliaga, M., Canchaya, S., Aranda, A., Ramirez, L., 1994. Estudio geovolcánico e inventario sistemático de manisfestaciones geotermales del lote Tutupaca. INGEMMET & ELECTROPERU, Lima, pp. I–3 (Informe Interno).
Sébrier, M., Soler, P., 1991. Tectonics and magmatism in the Peruvian Andes from late Oligocene time to the present. GSA (Geol. Soc. Am.) Spec. Pap. (Reg. Stud.) 265, 259–277.
Siebert, L., Simkim, T., Kimberly, P., 2011. Volcanoes of the World. 3. Ed. Washington, D.C.: Smithsonian Institution, Berkeley, CA. University of California Press, p. 551.
Steinmüller, K., 2001. Modern hot springs in the southern volcanic Cordillera of Peru and their relationship to Neogene epithermal precious-metal deposits. J. S. Am. Earth Sci. 14, 377–385.
Thouret, J.C., Davila, J., Eissen, J.P., 1999. Largest historic explosive eruption in the Andes at Huaynaputina volcano, south Peru. Geology 27, 435–438.
Thouret, J.C., Finizola, A., Fornari, M., Suni, J., Legeley-Padovani, A., Frechen, M., 2001. Geology of el Misti volcano nearby the city of arequipa, Peru. Geol. Soc. Am. Bull. 113, 1593–1610.
Thouret, J.C., Rivera, M., Wörner, G., Gerbe, M., Finizola, A., Fornari, M., Gonzales, K., 2005. Ubinas: the evolution of the historically most active volcano in southern Peru. Bull. Volcanol. 67, 557–589.
Thouret, J.C., Jicha, B.R., Paquette, J.L., Cubukcu, E.H., 2016. A 25 myr chronostratigraphy of ignimbrites in south Peru: implications for the volcanic history of the Central Andes. J. Geol. Soc. London 173, 734–756.
Tosdal, R.M., Farrar, E., Clark, A.H., 1981. K-Ar geocronology of the late cenozoic volcanic rocks of the Cordillera Occidental. Southern Perú. J. Volcanol. Geotherm. Res. 10, 157–173.
Valderrama, P., 2016. Origin and Dynamics of Volcanic Debris Avalanches: Surface Structure Analysis of Tutupaca Volcano (Peru). Université Blaise Pascal-Clermont II. https://tel.archives-ouvertes.fr/tel-01487051.
Valderrama, P., Roche, O., Samaniego, P., van Wyk de Vries, B., Bernard, K., Mariño, J., 2016. Dynamic implications of ridges on a debris avalanche deposit at Tutupaca volcano (southern Peru). Bull. Volcanol. 78, 1–11.
Valderrama, P., Roche, O., Samaniego, P., van Wyk de Vries, B., Araujo, G., 2018. Granular fingering as a mechanism for ridge formation in debris avalanche deposits: laboratory experiments and implications for Tutupaca volcano, Peru. J. Volcanol. Geoth. Res. 349, 409–418.
Valdivia, J.G., 1847. Fragmentos para la historia de Arequipa. Folletín de El Deber, Arequipa, pp. 109–111.
Van Wyk de Vries, B., Kerle, N., Petley, D., 2000. Sector collapse forming at Casita volcano. Nicaragua. Geol. 28, 167–170.
Van Wyk de Vries, B., Self, S., Francis, P.W., Keszthelyi, L., 2001. A gravitational spreading origin for the Socompa debris avalanche. J. Volcanol. Geoth. Res. 105, 225–247.
Van Wyk de Vries, B., Davis, T., 2015. Landslides, debris avalanches and volcanic gravitational deformation. In: Sigurdsson, H., Houghton, B., McNutt, S., Rymer, H., Stix, J. (Eds.), The Encyclopedia of Volcanoes, second ed., pp. 665–685.
Vidal, N., Merle, O., 2000. Reactivation of basement faults beneath volcanoes: a new model of flank collapse. J. Volcanol. Geoth. Res. 99, 9–26.
Zamácola y Jaúregui, J.D., 1804. Apuntes para la historia de Arequipa, vol. 49. Imp. De La Bolsa-Guañamarca, p. 1888.
Zech, R., Kull, Ch, Kubik, P.W., Viet, H., 2007. Exposure dating of late glacial and pre-LGM moraines in the cordon de Doña rosa, northern/Central Chile (~31°S). Clim. Past 3, 1–14.
Zerathe, S., Blard, P.H., Braucher, R., Bourlès, D., Audin, L., Carcaillet, J., Delgado, F., Benavente, C., Keddadouche, K., 2017. Toward the feldspar alternative for cosmogenic 10Be applications. Quat. Geochronol. 41, 83–96.

Supplementary data

Sample	Lat (dec°)	Lon (dec°)	Alt (masl)	Conc (at/g)	1s (at/g)	Shield. Corr	Density	Thickness (cm)	Er. (cm/yr)
TU 2	-17,04573	-70,342225	5033	3,22E+05	6,42E+04	0,994	2,60	3,0	0
TU 3	-17,04048	-70,348332	5142	2,35E+05	3,50E+04	0,968	2,60	4,0	0
TU 5	-17,048699	-70,342908	4900	2,77E+05	4,04E+04	0,982	2,60	4,0	0
TU 6	-17,05109	-70,339944	4901	2,71E+05	4,93E+04	0,980	2,60	5,0	0